



HAL
open science

An efficient covariant frame for the spherical shallow water equations: Well balanced DG approximation and application to tsunami and storm surge

Luca Arpaia, Mario Ricchiuto, Andrea Gilberto Filippini, Rodrigo Pedreros

► To cite this version:

Luca Arpaia, Mario Ricchiuto, Andrea Gilberto Filippini, Rodrigo Pedreros. An efficient covariant frame for the spherical shallow water equations: Well balanced DG approximation and application to tsunami and storm surge. *Ocean Modelling*, 2021, pp.101915. 10.1016/j.ocemod.2021.101915 . hal-03421078

HAL Id: hal-03421078

<https://inria.hal.science/hal-03421078>

Submitted on 9 Nov 2021

HAL is a multi-disciplinary open access archive for the deposit and dissemination of scientific research documents, whether they are published or not. The documents may come from teaching and research institutions in France or abroad, or from public or private research centers.

L'archive ouverte pluridisciplinaire **HAL**, est destinée au dépôt et à la diffusion de documents scientifiques de niveau recherche, publiés ou non, émanant des établissements d'enseignement et de recherche français ou étrangers, des laboratoires publics ou privés.

An efficient covariant frame for the spherical shallow water equations: well balanced DG approximation and application to tsunami and storm surge

Luca Arpaia¹, Mario Ricchiuto², Andrea Gilberto Filippini¹ and Rodrigo Pedreros¹

*Coastal Risk and Climate Change, French Geological Survey
3 Av. C. Guillermin 45060 Orléans Cedex 2, France*

*and
Team Cardamom - INRIA, Univ. Bordeaux, CNRS, Bordeaux INP, IMB, UMR 5251,
200 Avenue de la Vieille Tour, 33405 Talence cedex, France*

Abstract

In this work we consider an efficient discretization of the Shallow Water Equations in spherical geometry for oceanographic applications. Instead of the classical 2d-covariant or 3d-Cartesian approaches, we focus on the mixed 3d/2d form of [Bernard et al., JCP 2009] which evolves the 2d momentum tangential to the sphere by projecting the 3d-Cartesian right-hand side on the sphere surface. Differently from the last reference we consider the exact representation of the sphere instead of the finite element one, mixed with a covariant basis projection of the momentum. This leads to several simplifications of the Discontinuous Galerkin scheme: the local mass matrix goes back to the standard block-diagonal form; the Riemann Problem does not require any tensor or vector rotations to align the bases on the two sides of an edge. Second we consider well balancing corrections related to relevant equilibrium states for tsunami and storm surge simulations. These corrections allow to compensate for the inherent non-exactness of the quadrature induced by the non-polynomial nature of both the geometrical mapping and of the covariant basis. In other words, these corrections are the order of the cubature error. We show that their addition makes the scheme exactly well balanced, and is equivalent to recasting the integral of the hydrostatic pressure term in strong form. The proposed method is validated on academic benchmarks involving both smooth and discontinuous solutions, and applied to realistic tsunami and an historical storm surge simulation.

Keywords: shallow water equations, spherical geometry, discontinuous galerkin, well balanced schemes, tsunami, storm surge

Email address: l.arpaia@brgm.fr, mario.ricchiuto@inria.fr, a.filippini@brgm.fr, r.pedreros@brgm.fr (Luca Arpaia¹, Mario Ricchiuto², Andrea Gilberto Filippini¹ and Rodrigo Pedreros¹)

1. Introduction

Coastal flooding is mainly caused by meteorological and telluric phenomena which may occur at the scale of the oceanic basin. The numerical simulation of such events requires to solve the governing equations in a spherical geometry. In this work we consider the Shallow Water Equations (SWEs) which provide satisfactory results for long wave phenomena such as tide/storm surge and tsunami.

The literature devoted to discrete formulation of the SWEs on the sphere is quite large. Two methods have emerged in the past to deal with the Earth curvature. A common approach among contemporary ocean models consists in a two-dimensional parametrization of the sphere through a proper curvilinear coordinate system. Then the primitive or shallow water equations are written directly on the curved manifold meaning that all the differential operators are transformed in curvilinear coordinates. A metric source term arises from the space variation of the curvilinear vectors basis. The underlying equations in curvilinear coordinates are typically discretized on regular grids with finite differences/finite volume schemes. Regional models use the traditional latitude-longitude parametrization. Unfortunately for global ocean models, the latitude-longitude coordinate system has a singular point in the Arctic Ocean at the North Pole, where the meridians converge on water. The Jacobian of the coordinate transformation is not defined and moreover the singularity imposes a severe restriction on the maximum time step allowed for stability. Nowadays the pole problem is considered merely as an economical one [1]. In particular, meteorologists have used a variety of fixes to circumvent the singularity and all of such fixes employ multiple curvilinear coordinates defined on different patches covering the whole sphere, [2, 3]. Then a specific treatment of the flux term at the edges dividing the patches, where the tangent basis changes, is deployed: a rotation of momentum vector [4] or an orthonormalization of the Riemann Problem [5, 6] assure a common reference system at the edge and local conservation. To bypass the pole problem ocean modelers have used instead ad hoc curvilinear coordinates conceived to place the singularity point on lands, see for example the tripolar grid of [7]. Finally, for Finite Volume methods, some authors [6] claimed that extra care should be taken in the resolution of the Riemann Problem in curvilinear coordinates.

A second approach consists instead in resolving the governing PDEs in a three-dimensional Cartesian framework and then adding a constraint to force the currents to remain tangent to the sphere [8, 9]. With this approach, it is more common to represent the sphere approximately through a local finite element map for each element. Thanks to the local map, no special treatment is required in polar regions to preserve accuracy and to conserve global mass.

A third approach seems to combine the advantages of both methods [10]: momentum time derivative is written with respect to 2d components while the right-hand side is first expressed in 3d and then projected

33 back onto the sphere surface by a simple scalar product with respect to the tangent basis. The advantage
34 is that the number of unknown is kept to a minimum (water depth and two momentum components)
35 and, at the same time, the right-hand side maintains a Cartesian form, thus it is independent from the
36 parametrization of the sphere, and moreover there is no need to transform the differential operators. For
37 example, in tsunami applications this could be laborious for depth averaged non-hydrostatic models with
38 dispersive terms that involve mixed high order derivatives. If requested, Riemann solvers are formulated
39 easily in 3d Cartesian framework, and then projected on the sphere surface along with the right-hand side.
40 In the last reference the geometrical error related to the approximation of the curvature of the sphere is
41 controlled by using higher order super-parametric finite element approximations of the spherical geometry.

42 Here we present some improvements of the mixed 3d/2d formulation of [10] applied to spherical ge-
43 ometry. First we use an exact representation of the spherical elements, which allows to avoid the pole
44 problem altogether. A similar idea is used in the recent work by [11]. In our case, we then introduce a 2d
45 covariant representation of the momentum vector. This combination completely cancels the geometrical
46 error related to the sphere curvature. In practice, we can use any local reference mapping we want to
47 represent the 3d spatial coordinates, including the classical latitude longitude transformation. Due to
48 the orthogonality of covariant vector basis, the momentum equations remain decoupled as in the planar
49 case, which simplifies the structure of the update. Moreover, the Riemann solvers also simplify thanks
50 to continuity of the geometrical quantities as well as of the covariant basis at the elements edges. More
51 precisely, no rotations of the velocities/momentum components, nor averaging of the normals are required.

52 The discontinuous Galerkin (DG) method is becoming increasingly popular in geophysical fluid dy-
53 namics, proving also in this field its potential in terms of high order accuracy, conservation properties and
54 ease of massively parallel implementation. It has been applied to the spherical SWEs in different forms:
55 at the opposite ends of the spectrum we mention the purely two-dimensional form on the cubed sphere
56 [4] and the fully 3d Cartesian form on a finite elements quadrilateral grids [9]. Here we discretize the
57 spherical SWEs in the proposed 3d/2d-covariant form. Then we look to the well balanced property, or the
58 discrete preservation of some steady states which are of particular interest for tsunami and storm surge
59 computations. These states include the lake at rest, which results from the steady balance between hydro-
60 static pressure and the force played by the bottom and the inverse barometer in which the atmospheric
61 pressure effect is also added to the balance. In general well balanced methods are more robust and allow
62 to work with coarser mesh. A well balanced DG method typically relies on the fact that the so-called
63 strong form (with a second integration by parts of the volume flux term) embeds more easily than the
64 weak form the well balanced property at a discrete level. Based on the fact that the strong form is more

65 suited to retain well balancing, some authors ([12, 13]), while being stuck to the weak DG form (with
66 one integration by parts of the flux term), compute exactly the integrals in order to maintain a discrete
67 equivalence to the strong form. Other authors (see e.g. [14]) write directly the scheme in the strong form.
68 This has close similarities with fully residual based methods (see e.g. [15, 16]), and allows to obtain well
69 balancing independently on the quadrature formula used. Such flexibility is used to retain general well
70 balanced states on the sphere [17]. Here we start from the weak DG form and we show that, when applied
71 to the mixed 3d/2d formulation of the SWEs, it is unable to preserve equilibria due to inexactness of the
72 quadrature formula with non-polynomial functions as the ones contained in the components of the tangent
73 vectors. We add a well balancing correction related to relevant equilibrium states for tsunami and storm
74 surge simulations. These corrections involve the quadrature error. There are thus small by definition, and
75 compensate for the lack of summation by parts property making the scheme exactly well balanced. We
76 show that this idea is equivalent to recasting the integral of the hydrostatic pressure term in the strong
77 form.

78 The paper is organized as follows. In section 2 we introduce the notation for the spherical geometry.
79 In section 3 we introduce the SWEs in the 3d-2d covariant formulation. In section 4 we discuss their well
80 balanced DG approximation. In section 5 we detail computational aspects such as shock-capturing and
81 time-stepping. In section 6 we evaluate the proposed methods on standard global benchmarks for the
82 shallow water equations on the sphere and on regional realistic tsunami/storm surge computations.

83 2. Tangent maps for the sphere

84 We consider a sphere \mathcal{S}^2 with radius R described by generic curvilinear coordinates $\{X^1, X^2\}$ and
85 tangent basis $\{\mathbf{t}_1, \mathbf{t}_2\}$. The coordinate vector \mathbf{x} then writes:

$$\mathbf{x} = x^i \mathbf{e}_i \equiv x^1 \mathbf{e}_1 + x^2 \mathbf{e}_2 + x^3 \mathbf{e}_3 \quad (1)$$

$$= X^\alpha \mathbf{t}_\alpha \equiv X^1 \mathbf{t}_1 + X^2 \mathbf{t}_2 \quad (2)$$

Note that in the above definitions and in the following ones repeated indices imply summation. In particular, Latin indices are used for the components of vectors in Cartesian coordinates (from 1 to 3), while Greek indices are used for vectors in local curvilinear coordinates (from 1 to 2). The transformation from the curvilinear space to the physical space is defined here as $\mathbf{x} = T(\mathbf{X})$. It has a Jacobian or transformation tensor:

$$\mathbf{J}_T = \frac{\partial \mathbf{x}}{\partial \mathbf{X}} \quad (3)$$

with components $J_T^{i\alpha}$ and an inverse Jacobian:

$$\mathbf{J}_T^{-1} = \frac{\partial \mathbf{X}}{\partial \mathbf{x}} \quad (4)$$

86 with components $(J_T^{-1})^{\alpha i}$. The tangent vectors can be obtained by differentiation as the columns of the
87 Jacobian. It is useful to normalize the basis:

$$\mathbf{t}_\alpha = \frac{\partial \mathbf{x}}{\partial X^\alpha}, \quad \mathbf{t}_\alpha^* = \frac{\mathbf{t}_\alpha}{\|\mathbf{t}_\alpha\|} \quad (5)$$

in general $\mathbf{t}_\alpha^* \cdot \mathbf{t}_\beta^* \neq \delta_{\alpha\beta}$. Finally we define the metric tensor constructed from the Jacobian matrix as:

$$\mathbf{G} = \mathbf{J}_T^t \mathbf{J}_T \quad (6)$$

and $G = \det \mathbf{G}$, having denoted by t the matrix transpose. If the inverse Jacobian cannot be computed directly from the definition (4), it can be replaced by the pseudo-inverse:

$$\mathbf{J}_T^{-1} = \mathbf{G}^{-1} \mathbf{J}_T^t \quad (7)$$

88 Depending on the transformation, different representations of the spherical geometry can be obtained.

89 2.1. Finite Element map

T can be a local finite element transformation [9, 17] that maps a reference element to a spherical element, denoted by

$$E_K : K \rightarrow \mathcal{K}, \quad \mathbf{x} = \sum_{j \in \text{DOFs}} \varphi_j(\mathbf{X}) \mathbf{x}_j \quad (8)$$

90 where X_1, X_2 are the reference coordinates and \mathbf{x}_j are the physical coordinates of the degrees of freedom.
91 The Jacobian and the tangent vectors follow from the application of the definitions (3) and (5), while the
92 inverse Jacobian (4) has to be intended as the pseudo-inverse. A high order accurate geometry is usually
93 attained by increasing the polynomial degree of the basis functions φ_j .

94 2.2. Spherical map

95 In this work we will use the exact spherical transformation, defined here as:

$$G : [-\pi, +\pi] \times \left[-\frac{\pi}{2}, +\frac{\pi}{2}\right] \rightarrow \mathcal{S}^2, \quad \mathbf{x} = G(\mathbf{X}) \quad (9)$$

96 where

$$\begin{aligned} x^1 &= R \cos X_2 \cos X_1 \\ x^2 &= R \cos X_2 \sin X_1 \\ x^3 &= R \sin X_2 \end{aligned} \quad (10)$$

with X_1 the longitude and X_2 the latitude. Explicit expressions for the Jacobian, inverse Jacobian and tangent vectors follow from (3), (4), and (5). For example the Jacobian reads:

$$\mathbf{J}_G = \begin{bmatrix} -R \cos X^2 \sin X^1 & R \sin X^2 \cos X^1 \\ R \cos X^2 \cos X^1 & R \sin X^2 \sin X^1 \\ 0 & R \cos X^2 \end{bmatrix} \quad (11)$$

97 The tangent vectors are also called covariant vectors and they are denoted as $\mathbf{g}_\alpha = \frac{\partial \mathbf{x}}{\partial X^\alpha}$. Please note
 98 that the normalized covariant basis is orthonormal $\mathbf{g}_\alpha^* \cdot \mathbf{g}_\beta^* = \delta_{\alpha\beta}$. As already mentioned, the spherical
 99 transformation is singular at the poles.

100 An alternative and equivalent exact map that avoids the pole singularity but does not keep orthogonal-
 101 ity of the tangent basis is the following local transformation that maps a reference element to a spherical
 102 element:

$$A_K : K \rightarrow \mathcal{K}, \quad \mathbf{x} = R \frac{F(\mathbf{X})}{\|F(\mathbf{X})\|} \quad (12)$$

where $F = \sum_{j=1}^3 \varphi_j(\mathbf{X}) \mathbf{x}_j$ is the P1 finite element transformation from the reference element to the 3d
 element. The above transformation has a smooth Jacobian (3) everywhere:

$$\frac{\partial x^k}{\partial X^\alpha} = \frac{R}{\|F\|} \sum_{j=1}^3 \frac{\partial \varphi_j}{\partial X^\alpha} x_j^k - \frac{R \sum_{j=1}^3 \varphi_j(\mathbf{X}) x_j^k}{\|F\|^2} \frac{\partial \|F\|}{\partial X^\alpha} \quad (13)$$

103 from which we can compute the normalized tangent vectors with (5).

104 3. Shallow Water Equations in spherical geometry

105 We consider the SWEs in spherical geometry with uneven bathymetry and in presence of earth rotation.
 106 We express them in a generic vector form:

$$\frac{\partial h}{\partial t} + \nabla \cdot (h\mathbf{u}) = 0 \quad (14)$$

$$\frac{\partial h\mathbf{u}}{\partial t} + \nabla \cdot \mathbf{T} = \mathbf{S} \quad (15)$$

107 with h the fluid depth, $h\mathbf{u}$ the discharge/momentum vector, and having denoted the momentum flux tensor
 108 by \mathbf{T} . The source \mathbf{S} includes the effects of bathymetry, **bottom friction**, Coriolis force, and meteorological
 109 forcing:

$$\mathbf{S} = -gh\nabla b - c_F h\mathbf{u} - 2\Omega\mathbf{k} \times h\mathbf{u} - \frac{gh}{\rho_0} \nabla p_{atm} + f_w \quad (16)$$

110 In the formula above $b(\mathbf{x})$ denotes the bathymetry/topography, c_F the friction coefficient given by the
 111 Manning formula, Ω the Earth rotation rate and \mathbf{k} the Earth rotation axis. p_{atm} is the atmospheric
 112 pressure, ρ_0 is the water density and f_w represents the wind forcing. Turbulent eddy viscosity term has
 113 been neglected.

114 The expressions of nabla $\nabla \cdot$, of the momentum vector $h\mathbf{u}$ and of the tensor \mathbf{T} depend on the coordi-
 115 nate system in which they are expressed. The most common representations used for the shallow water
 116 equations are either the 3d Cartesian coordinates or the curvilinear coordinates defined in section 2. The
 117 momentum vector $h\mathbf{u}$ can be expressed in both systems (see (1) and (2)) as:

$$h\mathbf{u} = hu^i \mathbf{e}_i \equiv hu^1 \mathbf{e}_1 + hu^2 \mathbf{e}_2 + hu^3 \mathbf{e}_3 \quad (17)$$

$$= hu^\alpha \mathbf{t}_\alpha \equiv hu^{\alpha 1} \mathbf{t}_1 + hu^{\alpha 2} \mathbf{t}_2 \quad (18)$$

118 We remark that, for curvilinear coordinates, momentum components are not defined in a unitary basis.
 119 It may be convenient expressing momentum in a unitary basis:

$$h\mathbf{u} = hu^\alpha \frac{\mathbf{t}_\alpha}{\|\mathbf{t}_\alpha\|} \quad (19)$$

$$= hu^{*\alpha} \mathbf{t}_\alpha^* \quad (20)$$

120 The relationship between the velocity components written in the two basis is:

$$u^i = J_T^{i\alpha} u^\alpha, \quad u^i = J_T^{*,i\alpha} u^{*\alpha} \quad (21)$$

121 where $J_T^{*,i\alpha} = J_T^{i\alpha} / \|\mathbf{t}_\alpha\|$ (repeated index summation does not apply here) is the Jacobian (3) normalized
 122 by columns. Similarly the second order flux tensor \mathbf{T} can be expressed in both coordinate systems as:

$$\mathbf{T} = T^{ij} \mathbf{e}_i \mathbf{e}_j \quad (22)$$

$$= T^{\alpha\beta} \mathbf{t}_\alpha \mathbf{t}_\beta \quad (23)$$

123 with Cartesian components $T^{ij} = hu^i u^j + P\delta_{ij}$ and curvilinear components $T^{\alpha\beta} = hu^\alpha u^\beta + GP\delta_{\alpha\beta}$. The
 124 hydrostatic pressure is defined as $P = gh^2/2$ and G is the determinant of the metric tensor (6).

125 3.1. Equilibrium states

126 For coastal flows, an important role is played by the so-called *lake at rest* state which, denoting the
 127 free surface level $\eta = h + b$, is the particular steady solution characterized by the two invariants (18):

$$h\mathbf{u} = 0, \quad Z = \eta = const = Z_0 \quad (24)$$

128 In presence of atmospheric pressure forcing, a relevant state is the *inverted barometer* balance that is an
 129 exact solution of the SWEs in case of full adjustment of sea level to changes in barometric pressure [19]:

$$h\mathbf{u} = 0, \quad Z = \eta + \frac{p_{atm}}{g\rho_0} = const = Z_1 \quad (25)$$

130 Full adjustment is never reached since the pressure field is unsteady $p_{atm}(\mathbf{x}, t)$, thus one may question if
 131 this is really a relevant equilibrium, but it is interesting to be able to handle this possibility numerically.
 132 In [20] it has been shown that, at least in deep water, the free surface response is almost isostatic and
 133 characterized by small perturbations around the inverted barometer balance. In light of these findings
 134 and for completeness, we have investigated the more general balance (25).

135 A numerical method approximating (14)-(15) is said to be well balanced if (24) or (25) are also exact
 136 solutions of the discrete equations. In other words, well balanced schemes provide a discrete analog of the
 137 balance between hydrostatic pressure and the forces exerted by the bottom (and by atmospheric pressure)

$$\nabla \cdot P\mathbf{I} = -gh\nabla \left(b + \frac{p_{atm}}{g\rho_0} \right) \quad (26)$$

138 3.2. Fully diagonal mixed 3d/2d-covariant formulation

139 Following [10] we proceed as follows to obtain the fully discrete equations.

140 1. we project the momentum equation (15), on the tangent plane:

$$\frac{\partial}{\partial t}(h\mathbf{u} \cdot \mathbf{t}_\alpha^*) + (\nabla \cdot \mathbf{T}) \cdot \mathbf{t}_\alpha^* = \mathbf{S} \cdot \mathbf{t}_\alpha^*$$

141 2. the scalar product contained in the time derivative is performed with momentum expressed in
 142 curvilinear coordinates while the scalar product involving the rest of the equation is performed in
 143 3d Cartesian coordinates:

$$\begin{aligned} & \frac{\partial}{\partial t}(hu^{*\beta}t_\beta^{*j}t_\alpha^{*j}) + \frac{\partial T^{jk}}{\partial x^k}t_\alpha^{*j} = S^jt_\alpha^{*j} \\ \text{e.g. } (\alpha = 1) & \quad \frac{\partial}{\partial t}(hu^{*1}\mathbf{t}_1^* \cdot \mathbf{t}_1^* + hu^{*2}\mathbf{t}_2^* \cdot \mathbf{t}_1^*) + \left(\frac{\partial T^{11}}{\partial x^1} + \frac{\partial T^{12}}{\partial x^2} + \frac{\partial T^{13}}{\partial x^3} \right) t_1^{*1} \\ & \quad + \left(\frac{\partial T^{21}}{\partial x^1} + \frac{\partial T^{22}}{\partial x^2} + \frac{\partial T^{23}}{\partial x^3} \right) t_1^{*2} \\ & \quad + \left(\frac{\partial T^{31}}{\partial x^1} + \frac{\partial T^{32}}{\partial x^2} + \frac{\partial T^{33}}{\partial x^3} \right) t_1^{*3} = S^jt_1^{*j} \end{aligned} \quad (27)$$

144 One advantage of this formulation with respect to full 3d equations is that the number of unknowns
 145 is kept minimum (h, hu^1, hu^2) . Another attractive feature is that the flux function stays in 3d form and
 146 does not depend on a particular transformation. This means that line integrals are defined intrinsically

147 and mass is easily conserved circumventing implementation issue related to the use of composite meshes
 148 in the 2d approach. The drawback of this formulation compared to the fully two-dimensional one is that
 149 for each momentum equation 9 components of the fluxes have to be evaluated instead of three, and that
 150 in general the curvilinear momentum components are coupled.

151 However, differently from [10] we propose to use the exact spherical representation, thus we have to
 152 project momentum on the exact tangent basis. We can choose either the covariant framework [10] or the
 153 local transformation [12]. Here we have used locally in each element the covariant framework guaranteeing
 154 the decoupling of the momentum components, and for which simple analytical expressions exist for the
 155 tangent vectors $\mathbf{g}_\alpha = \frac{\partial \mathbf{x}}{\partial X^\alpha}$. We project onto the normalized tangent basis [5] to get:

$$\frac{\partial}{\partial t}(h\mathbf{u} \cdot \mathbf{g}_\alpha^*) + (\nabla \cdot \mathbf{T}) \cdot \mathbf{g}_\alpha^* = \mathbf{S} \cdot \mathbf{g}_\alpha^* \quad (28)$$

156 or by components (e.g. $\alpha = 1$):

$$\begin{aligned} \frac{\partial}{\partial t}(hu^{*1} \underbrace{\mathbf{g}_1^* \cdot \mathbf{g}_1^*}_{=1} + hu^{*2} \underbrace{\mathbf{g}_2^* \cdot \mathbf{g}_1^*}_{=0}) + \left(\frac{\partial T^{11}}{\partial x^1} + \frac{\partial T^{12}}{\partial x^2} + \frac{\partial T^{13}}{\partial x^3} \right) g_1^{*1} \\ + \left(\frac{\partial T^{21}}{\partial x^1} + \frac{\partial T^{22}}{\partial x^2} + \frac{\partial T^{23}}{\partial x^3} \right) g_1^{*2} \\ + \left(\frac{\partial T^{31}}{\partial x^1} + \frac{\partial T^{32}}{\partial x^2} + \frac{\partial T^{33}}{\partial x^3} \right) g_1^{*3} = S^j g_1^{*j} \end{aligned}$$

157 So in practice we work with:

$$\frac{\partial}{\partial t}(hu^{*\alpha}) + \frac{\partial T^{jk}}{\partial x^k} g_\alpha^{*j} = S^j g_\alpha^{*j} \quad (29)$$

158 This choice allows to take advantage of the orthogonality of the covariant basis and work with a fully
 159 diagonal system which is the main advantage of the formulation proposed here. Please note also that this
 160 algorithm evolves physical components of momentum $hu^{*\alpha}$ in m^2/s (eastward for $\alpha = 1$, and northward
 161 for $\alpha = 2$).

162 4. Well balanced discontinuous finite element discretization

We consider a discretization of \mathcal{S}^2 composed by non overlapping triangular elements \mathcal{K} . To each element \mathcal{K} we can associate an element defined in the parametric space, which we denote by K . For a given mesh, we label by the roman h the characteristic mesh size measured in physical space. Following a high order DG procedure, we project the vector of conserved variables and the bathymetry into the finite dimensional space:

$$V_h^p = \{\varphi : \varphi(\mathbf{x}) \in L_K^p, \mathbf{x} \in K\} \quad (30)$$

163 where L_K^p are Lagrange polynomials of degree p defined on each parametric element K . We obtain the
 164 weak formulation multiplying the mass equation (14) and the momentum equation (28) by a smooth test
 165 function φ_i that belongs to the same space (30) and integrating it on a spherical triangle \mathcal{K} :

$$\frac{\partial}{\partial t} \int_{\mathcal{K}} h_{\text{h}} \varphi_i \, d\mathbf{x} + \int_{\partial\mathcal{K}} h \mathbf{u}_{\text{h}}^{\text{Y}} \varphi_i \cdot \mathbf{n} \, ds - \int_{\mathcal{K}} h \mathbf{u}_{\text{h}} \cdot \nabla \varphi_i \, d\mathbf{x} = 0 \quad (31)$$

$$\frac{\partial}{\partial t} \int_{\mathcal{K}} h \mathbf{u}_{\text{h}} \cdot \mathbf{g}_{\alpha}^* \varphi_i \, d\mathbf{x} + \int_{\partial\mathcal{K}} \mathbf{T}_{\text{h}}^{\text{Y}} \mathbf{g}_{\alpha}^* \varphi_i \cdot \mathbf{n} \, ds - \int_{\mathcal{K}} \mathbf{T}_{\text{h}} : \nabla (\mathbf{g}_{\alpha}^* \varphi_i) \, d\mathbf{x} = \int_{\mathcal{K}} \mathbf{S}_{\text{h}} \cdot \mathbf{g}_{\alpha}^* \varphi_i \, d\mathbf{x} \quad (32)$$

166 where $\mathbf{T}_{\text{h}}^{\text{Y}}$ denotes the numerical flux evaluated at the elements boundaries, and the symbol $:$ is the scalar
 167 product between second order tensors $\mathbf{A} : \mathbf{B} = A_{ij} B_{ji}$. As noted in [10], if we regroup $\mathbf{g}_{\alpha}^* \varphi_i = \mathbf{v}_{i,\alpha}$, then
 168 (32) corresponds to consider a vectorial test function for each momentum equation.

169 Several aspects need to be clarified. First of all the mapping required to define the quadrature formulas,
 170 which will involve non-algebraic transformations. Secondly, the well balancedness w.r.t the equilibria
 171 presented earlier is not trivial in this formulation as exact quadrature is impossible precisely due to the
 172 non-algebraic nature of the mappings adopted. These aspects are covered in the next sections.

173 4.1. Reference element mapping and quadrature

174 All the integrals are computed on the standard reference triangle K . For the transformation which
 175 map a reference triangle to a spherical triangle we use (12), which allows to bypass the pole singularity in
 176 the evaluation of the integral and the differential operators. Consider for example the volume integral in
 177 the momentum equation which we decompose into

$$\begin{aligned} \int_{\mathcal{K}} \mathbf{T}_{\text{h}} : \nabla (\mathbf{g}_{\alpha}^* \varphi_i) \, d\mathbf{x} &= \int_{\mathcal{K}} T_{\text{h}}^{kj} \frac{\partial}{\partial x^k} (g_{\alpha}^{*j} \varphi_i) \, d\mathbf{x} \\ &= \int_{\mathcal{K}} T_{\text{h}}^{kj} \varphi_i \frac{\partial g_{\alpha}^{*j}}{\partial x^k} \, d\mathbf{x} + \int_{\mathcal{K}} T_{\text{h}}^{kj} g_{\alpha}^{*j} \frac{\partial \varphi_i}{\partial x^k} \, d\mathbf{x} \end{aligned} \quad (33)$$

178 Both the resulting integrals are mapped using (12), so the differential is rescaled based on the mapping
 179 Jacobian

$$d\mathbf{x} = J_A \, d\mathbf{X}. \quad (34)$$

180 with $J_A = \sqrt{G}$ and $G = \det(\mathbf{J}_A^t \mathbf{J}_A)$, see (6). The derivatives of the test functions are evaluated classically
 181 via the gradient in the mapped element as

$$\frac{\partial}{\partial x^k} = \frac{\partial X^{\beta}}{\partial x^k} \frac{\partial}{\partial X^{\beta}} = (\mathbf{J}_A^{-1})^{\beta k} \frac{\partial}{\partial X^{\beta}} \quad (35)$$

with the inverse Jacobian $\mathbf{J}_A^{-1} = \mathbf{G}^{-1} \mathbf{J}_A^t$, see (7). All the remaining quantities are evaluated analytically
 via the mapping (12), including the gradients of the covariant basis vectors, which can be easily obtained

analytically starting from (11) Line integrals are evaluated similarly via a mapping to a reference 1d element. As already remarked, for the the time derivative we can write

$$\frac{\partial}{\partial t} \int_{\mathcal{K}} h \mathbf{u}_h \cdot \mathbf{g}_\alpha^* \varphi_i d\mathbf{x} = \sum_{j \in \text{DOFs}} \int_{\mathcal{K}} \varphi_i \varphi_j d\mathbf{x} \frac{\partial h u_j^{*\alpha}}{\partial t} \quad (36)$$

which shows that a fully block diagonal structure is retained.

As a final remark, we note that differently from two-dimensional formulations, the right-hand side appears in Cartesian form and it is well-posed on the whole sphere. However the tangent basis in (32) is not well defined at the poles, for the latitude-longitude parametrization that we have chosen. For this reason, only to evaluate the tangent basis and its derivatives, a polar cap defined by a limiting latitude z_{lim} , is deployed. Elements are flagged according to the baricenter position: if $z_G^K > z_{\text{lim}}$ we use a rotated spherical transformation replacing (10) with:

$$\begin{aligned} x^1 &= R \cos X_2 \cos X_1 \\ x^2 &= -R \sin X_2 \\ x^3 &= R \cos X_2 \sin X_1 \end{aligned} \quad (37)$$

The Jacobian (3), inverse Jacobian (4) and basis vectors (5) are modified accordingly. Note that this is only affecting the local representation of the 3d basis which remains perfectly continuous across element edges. We found that the DG framework is well suited to handle such discontinuity at the elements edges with no modification necessary to the algorithm. In particular:

- each element updates the momentum components $h u^{*\alpha}$ in its own reference system, thus zonal/meridional components in standard elements and rotated components in polar cap elements.
- in a DG method, communication between elements is needed only for evaluating numerical fluxes. Since they are computed in a 3d framework (and independent from the local coordinate system) no specific treatment is necessary at the edges separating the polar cap.

In practice we have set $z_{\text{lim}} = 0.9R$, however we will show that this value has no impact on the numerical results.

4.2. Integration by parts correction

We are interested in the well-balanced nature of the scheme. We will first consider the lake at rest case. The effect of the atmospheric pressure is added introducing an apparent topography [21] $b \rightarrow B = b + \frac{p_{\text{atm}}}{g\rho_0}$.

Imposing the lake at rest, the momentum components of the DG method reduce to:

$$\int_{\partial\mathcal{K}} P_h^Y \mathbf{I} \mathbf{g}_\alpha^* \varphi_i \cdot \mathbf{n} ds - \int_{\mathcal{K}} P_h \mathbf{I} : \nabla (\mathbf{g}_\alpha^* \varphi_i) d\mathbf{x} = - \int_{\mathcal{K}} gh_h \nabla b \cdot \mathbf{g}_\alpha^* \varphi_i d\mathbf{x} \quad (38)$$

One drawback of the mixed formulation emerges: well balancing is lost because of the projection on the tangent basis, an operation that involves the evaluation of non-algebraic functions in all of the three integrals of (38). Indeed even with constant bathymetry, and constant pressure, in general we cannot remove the geometrical integration error

$$\epsilon_{P_0}^K = P_0 \left[\int_{\mathcal{K}} \mathbf{I} : \nabla (\mathbf{g}_\alpha^* \varphi_i) d\mathbf{x} - \int_{\partial\mathcal{K}} \mathbf{I} \mathbf{g}_\alpha^* \varphi_i \cdot \mathbf{n} ds \right] \quad (39)$$

This is an issue already encountered on curved finite element (polynomial) meshes [22], and is even more critical for the non-polynomial approximation used here. We remark that this was also highlighted in [17] in the context of the study of the well balancing of a fully 3d DG shallow water approximation on the sphere. As observed in the last reference, a more suitable form to guarantee the well balanced character of the method is the strong form. We obtain a somewhat similar result here, but we proceed in a different manner, and finally only the pressure term is converted into the strong form. Our idea is to balance the scheme with a small correction which is within the quadrature error, and thus much smaller than the truncation error of the scheme. To achieve this we re-inject into the scheme [32] the integration by parts error associated to the pressure terms, given by

$$\epsilon_P^K = \int_{\mathcal{K}} P_h \mathbf{I} : \nabla (\mathbf{g}_\alpha^* \varphi_i) d\mathbf{x} - \int_{\partial\mathcal{K}} P_h \mathbf{I} \mathbf{g}_\alpha^* \varphi_i \cdot \mathbf{n} ds + \int_{\mathcal{K}} (\nabla \cdot P_h \mathbf{I}) \cdot \mathbf{g}_\alpha^* \varphi_i d\mathbf{x} \quad (40)$$

202 Note that this term is identically zero for exact quadrature, and reduces to [39] if the pressure is con-
 203 stant. Note also that the only ansatz made is that P_h is the pressure associated to the finite element
 204 polynomial projection, and in our specific case P_h it is assumed to be a polynomial of degree $2p$, thus
 205 infinitely differentiable. We can characterize the correction term with the following property.

206

Proposition (*IBP correction bounds*) Let [40] be evaluated by means of quadrature formulas which are exact for polynomials of degree $k_{\mathcal{K}}$ for the volume integrals and $k_{\partial\mathcal{K}}$ for the boundary integral. The correction can be bounded as

$$\|\epsilon_P^K\| \leq C_{\mathcal{K}} h^{\min(k_{\partial\mathcal{K}}+1, k_{\mathcal{K}}+1)} \quad (41)$$

207

The proof of the above property is reported in the appendix. In practice, we have computed all integrals
 208 with formulas exact for $k_{\mathcal{K}} = k_{\partial\mathcal{K}} = 3p$. A numerical verification of the proposition for these choices is
 209 also reported in the appendix. When [40] is added to the discrete momentum equation, the variational

210 form becomes

$$\frac{\partial}{\partial t} \int_{\mathcal{K}} h_h \varphi_i \, d\mathbf{x} + \int_{\partial\mathcal{K}} h \mathbf{u}_h^\gamma \varphi_i \cdot \mathbf{n} \, ds - \int_{\mathcal{K}} h \mathbf{u}_h \cdot \nabla \varphi_i \, d\mathbf{x} = 0 \quad (42)$$

$$\frac{\partial}{\partial t} \int_{\mathcal{K}} h \mathbf{u}_h \cdot \mathbf{g}_\alpha^* \varphi_i \, d\mathbf{x} + \int_{\partial\mathcal{K}} \mathbf{T}_h^\gamma \mathbf{g}_\alpha^* \varphi_i \cdot \mathbf{n} \, ds - \int_{\mathcal{K}} \mathbf{T}_h : \nabla (\mathbf{g}_\alpha^* \varphi_i) \, d\mathbf{x} = \int_{\mathcal{K}} \mathbf{S}_h \cdot \mathbf{g}_\alpha^* \varphi_i \, d\mathbf{x} + \epsilon_P^K \quad (43)$$

211 4.3. Numerical fluxes: mass conservation and well balanced with discontinuous data

212 For the mixed 3d/2d formulation, all geometrical quantities are uniquely and objectively defined in
 213 3d, so we can use practically any Riemann solver in 3d Cartesian coordinates. The line integral in the
 214 momentum equation (32) reads:

$$\int_{\partial\mathcal{K}} \mathbf{T}_h^\gamma \cdot \mathbf{g}_\alpha^* \varphi_i \cdot \mathbf{n} \, ds = \int_{\partial\mathcal{K}} \underbrace{\mathbf{T}_h^\gamma \cdot \mathbf{n}}_H \cdot \mathbf{g}_\alpha^* \varphi_i \, ds \quad (44)$$

215 where $\mathbf{H} \in \mathbb{R}^3$ is a specified numerical flux $\mathbf{H}(\mathbf{u}_L, \mathbf{u}_R)$ and \mathbf{u}_L and \mathbf{u}_R are the left (internal) and the right
 216 (external) states $\mathbf{u} = \{h, hu^i\}$. In practice we use the Lax-Friedrich flux.

217 We remark that the problem of using a common framework between the left and right state in the
 218 original [10] is no longer necessary since the normals are continuous at the edges. Only a change of basis
 219 is needed at this point to compute 3d velocities because they are only available from momentum update,
 220 in 2d. This is done with the right relationship in (21) and the definition of the sphere Jacobian (3). The
 221 important consequence of this is that the method proposed conserves mass exactly without any special
 222 treatment of the normals on element boundaries.

223 To recover also the well balanced property in presence of discontinuous data, besides the addition of
 224 the hydrostatic correction in (43), as in [13] we evaluate the numerical flux at a reconstructed state \mathbf{u}^*
 225 [23] and add a high order correction term. The resulting well balanced mass/momentum numerical flux
 226 (distinguished by $\hat{\cdot}$) reads:

$$H = H(\mathbf{u}_L^*, \mathbf{u}_R^*) \quad (45)$$

$$\hat{\mathbf{H}} = \mathbf{H}(\mathbf{u}_L^*, \mathbf{u}_R^*) + (P(h_L) - P(h_L^*)) \mathbf{n} \quad (46)$$

227 for the definition of the reconstructed state $\mathbf{u} = \{h^*, h^* u^{*i}\}$ please refer to [23]. A strategy for recovering
 228 a well balanced scheme in presence of discontinuous data for the bathymetry on non-conforming elements
 229 is also discussed in [17]. In real applications, discontinuous data b, p_{atm} arise, for example, when the
 230 correspondent fields are computed at the degrees of freedom from a local minimization problem. For the
 231 bathymetry this can be beneficial to avoid Gibbs phenomena when data is nearly discontinuous on one cell
 232 and the polynomial order is $p > 1$. For the atmospheric pressure field we assume that it is continuously

233 interpolated at the degrees of freedom. In this case the well balanced correction related to the inverted
 234 barometer (first line is mass correction, second line is momentum correction):

$$+\frac{1}{2} \frac{1}{g\rho_0} \begin{pmatrix} \alpha_{LF} \\ g \frac{h_R^* + h_L^*}{2} \mathbf{n} \end{pmatrix} (p_{atm,L} - p_{atm,R}) \quad (47)$$

235 is identically zero, being $p_{atm,L} = p_{atm,R}$.

236 **Proposition.** (Well balanced) The mixed 3d/2d-covariant DG method (42) (43) with numerical fluxes
 237 (46) is well balanced in the sense that it preserves to machine accuracy initial data verifying (24) or (25).

Proof. The main assumption is that either $h_h + b_h = \eta_0 = \text{const}$, or $h_h + b_h + (p_{atm}/(g\rho_0))_h = \eta_0 = \text{const}$, within each cell. For the lake at rest state the flux reduces to $\mathbf{T}_h = P_h \mathbf{I}$. Then the discrete momentum equation (43) reduces to:

$$\int_{\partial\mathcal{K}} \left(\hat{\mathbf{H}} - P_h \mathbf{I} \cdot \mathbf{n} \right) \cdot \mathbf{g}_\alpha^* \varphi_i ds + \int_{\mathcal{K}} (\nabla \cdot P_h \mathbf{I}) \cdot \mathbf{g}_\alpha^* \varphi_i d\mathbf{x} = - \int_{\mathcal{K}} g h_h \nabla b \cdot \mathbf{g}_\alpha^* \varphi_i d\mathbf{x} \quad (48)$$

where we have canceled the first term of the correction (40) with the third term in (43) since they are equal and with opposite sign. Similarly to (13), the proof is based on the fact that, in the lake at rest case, the Lax-Friedrich flux evaluated at the reconstructed state is $\mathbf{H}(\mathbf{u}_L^*, \mathbf{u}_R^*) = P_h(h_L^*)$ and one can check that the well balanced numerical flux thus simplifies as $\hat{\mathbf{H}}(\mathbf{u}_L^*, \mathbf{u}_R^*) = P_h(h_L) \mathbf{I} \cdot \mathbf{n}$. Since the left state is the internal state we can further write $P_h(h_L) \mathbf{I} \cdot \mathbf{n} = P_h \mathbf{I} \cdot \mathbf{n}$. Then the integrand of the first term in (48) cancels out at each quadrature point and the whole penalization term vanishes. Moreover, for any order $h_h, b_h \in V_h^p$ on can show that:

$$\nabla \cdot P_h \mathbf{I} + g h_h \nabla b_h = \nabla \frac{g(\sum_j \varphi_j h_j)^2}{2} + g h_h \nabla b_h = g h_h \nabla \eta_h \quad (49)$$

238 With $h_h + b_h = \eta_0 = \text{const}$, also the volume terms in (48) cancel exactly, recovering the well balanced
 239 property. The same arguments holds for the inverted barometer case but replacing b with $B = b + \frac{p_{atm}}{g\rho_0}$
 240 \square .

241 5. Computational details

242 5.1. Shock capturing

The applications considered in this work may involve the formation of discontinuous solutions during the computation. For tsunami simulations, wave breaking occurring in shallow areas can cause the linear DG method to develop unphysical oscillations that eventually grow in time. We cope with the possibility

of non-smooth solutions with an entropy viscosity approach [24, 25] which consists in adding a diffusion-like term to the right-hand side of (14), (15). Here we discuss the details related to the implementation of the diffusive term in a spherical geometry. We consider only momentum equation since mass equation is a particular case. Given a diffusive flux tensor $\mathbf{G} = \mu \nabla h \mathbf{u}$, the DG discretization in the mixed formulation of section 3.2 writes:

$$\mathcal{I}_\mu := \int_{\mathcal{K}} \nabla \cdot \mathbf{G}_h \cdot \mathbf{g}_\alpha^* \varphi_i \, d\mathbf{x} = \int_{\partial\mathcal{K}} \mathbf{G}_h \cdot \mathbf{n} \cdot \varphi_i \mathbf{g}_\alpha^* \, ds - \int_{\mathcal{K}} \mathbf{G}_h : \nabla (\mathbf{g}_\alpha^* \varphi_i) \, d\mathbf{x} \quad (50)$$

To stabilize the shocks only the volume integral is retained and moreover we neglect the variation of the tangent basis so that integral (50) simplifies to:

$$\mathcal{I}_\mu = - \int_{\mathcal{K}} G_h^{kj} g_\alpha^{*j} \frac{\partial \varphi_i}{\partial x^k} \, d\mathbf{x} \quad (51)$$

Note that $G^{kj} g_\alpha^{*j} = G^{\alpha k}$ is a diffusive flux tensor projected on the tangent plane. As for the advective flux, since we evolve momentum in the tangent basis, we do not have access directly to G^{kj} in Cartesian basis. However the diffusive tensor components are easily recovered from relationships (21) and (35):

$$G^{kj} = \mu \frac{\partial h u^j}{\partial x^k} = \mu \frac{\partial}{\partial x^k} \left(J_G^{*,j\beta} h u^{*\beta} \right) = \mu h u^{*\beta} \frac{\partial g_\beta^{*j}}{\partial x^k} + \mu J_G^{*,j\beta} \frac{\partial h u^{*\beta}}{\partial x^k} \quad (52)$$

243 Near the discontinuities the viscosity coefficient μ should be of order h_K in order to kill oscillations while
 244 in smooth regions it is expected to be below the approximation order. To this end, we follow the principles
 245 originally proposed e.g. in [24, 25] and define this coefficient starting from the total energy residual. We
 246 refer to the last references for the formulation, and to [26] and references therein for its parametrization.

247 5.2. Time stepping

High order temporal accuracy is achieved, as it is standard, with a SSPRK method [27]. The time step is computed according to:

$$\Delta t = CFL \frac{\min_{\mathcal{K}} \rho_{\mathcal{K}}}{2 \max_f \alpha_{LF_f}} \quad (53)$$

248 with $\rho_{\mathcal{K}}$ the elemental inscribed circle radius and α_{LF_f} the Lax-Friedrich parameter at face f . For linear
 249 stability reason one should use $CFL = \frac{1}{2p+1}$ (being p the polynomial order of the approximation), but for
 250 practical use in this work we always set $CFL = 0.5$. For stability reasons, when included the Manning
 251 friction term is treated via a semi-implicit splitting as e.g. in [28, 29].

252 **6. Results**

253 In all computations presented hereafter we have set, unless otherwise stated, $R = 6371.22 \times 10^3 m$,
 254 $g = 9.80616 m^2 s^{-1}$, $\Omega = 7.295 \times 10^{-5} s^{-1}$ and $\rho_0 = 1025 kg/m^3$. Simulations have been carried out with
 255 linear (P^1), quadratic (P^2) and cubic polynomials (P^3).

256 *6.1. Global atmospheric tests*

257 In this paragraph we test the DG scheme on some classical benchmarks taken from the test suite of
 258 Williamson et al. (W92) [30] and [31].
 259 Global Steady-State Nonlinear Zonal Geostrophic Flow. *W92 Case #2* is an exact steady geostrophic
 260 equilibrium allowing to measure the order of accuracy in presence of Earth rotation. The velocity and
 261 height fields are initially given by:

$$\begin{aligned} h(\varphi, \lambda) &= h_0 - \frac{1}{g} \left(\Omega R u_0 + \frac{u_0^2}{2} \right) (-\cos \lambda \cos \varphi \sin \alpha + \sin \lambda \cos \alpha)^2 \\ u^{*1}(\varphi, \lambda) &= u_0 (\cos \lambda \cos \alpha + \cos \varphi \sin \lambda \sin \alpha) \\ u^{*2}(\varphi, \lambda) &= -u_0 \sin \varphi \sin \alpha \end{aligned} \quad (54)$$

262 with $gh_0 = 2.94 \times 10^4 m^2 s^{-2}$ and $u_0 = \frac{2\pi R}{12 days}$ and $\alpha = 0$. Grid convergence studies have been conducted on
 263 5 icosahedral grids, from level 1 ($h_K = 3571 km$) to level 5 ($h_K = 223 km$). Relative errors are evaluated
 264 following [30]:

$$e_p = \frac{\|e\|_{L^p}}{\|h_{ex}\|_{L^p}} \quad (55)$$

265 with $e = h - h_{ex}$ and h_{ex} the exact solution. The errors obtained at day 5 are reported on table [1]
 266 below. Convergence curves are compared in figure [1] against the results of the original [10]. To make the
 267 comparison effective, only for this experiment, we have tried to stick to their same scheme, DG in the
 268 weak-form [32] with Lax-Friedrich flux. We have remarked that the use of the well balanced momentum
 269 form [43] has almost no impact on the errors. The theoretical order of convergence has been obtained,
 270 with smaller errors with respect to the reference. We explain this improvement by the cancellation of the
 271 geometrical error in the sphere representation. As it is customary we report on figure [2] the error maps
 272 after 5 days of simulation on the fourth grid ($h_K = 446 km$).

Zonal Flow over an Isolated Mountain. *W92 Case #5* is a perturbation of the previous test. The initial
 velocity and height fields are equal to [54] with $\alpha = 0$, $h_0 = 5960 m$ and $u_0 = 20 m/s$. An isolated
 mountain is added:

$$b = b_0 \left(1 - \frac{r}{R} \right) \quad (56)$$

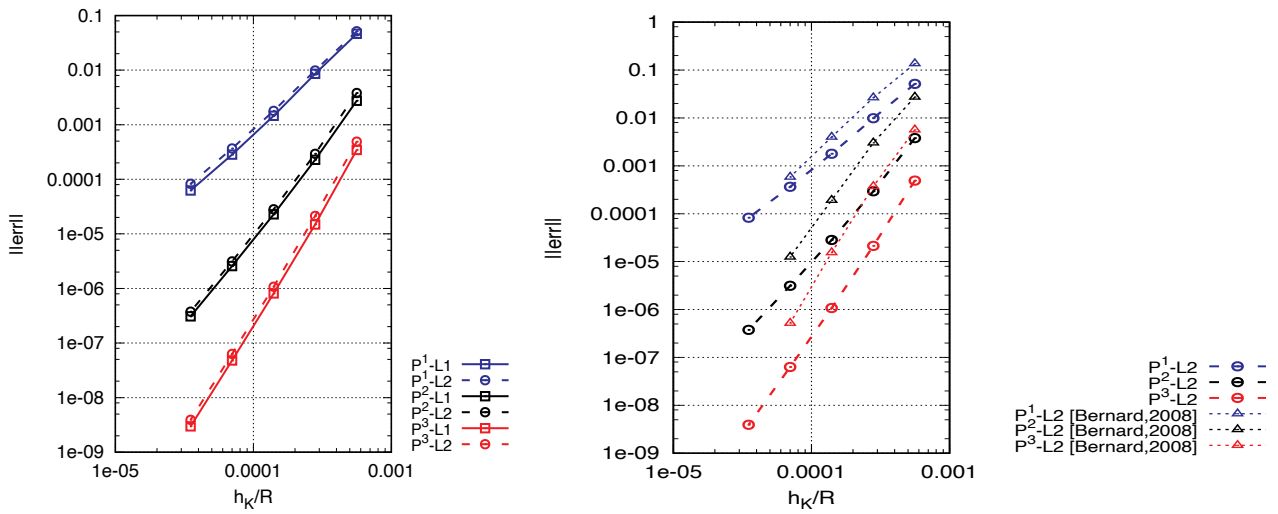


Figure 1: Global Steady-State Nonlinear Zonal Geostrophic Flow. Left: mesh convergence for L1 and L2 error norm. Right: mesh convergence for L2 error and comparison with [10].

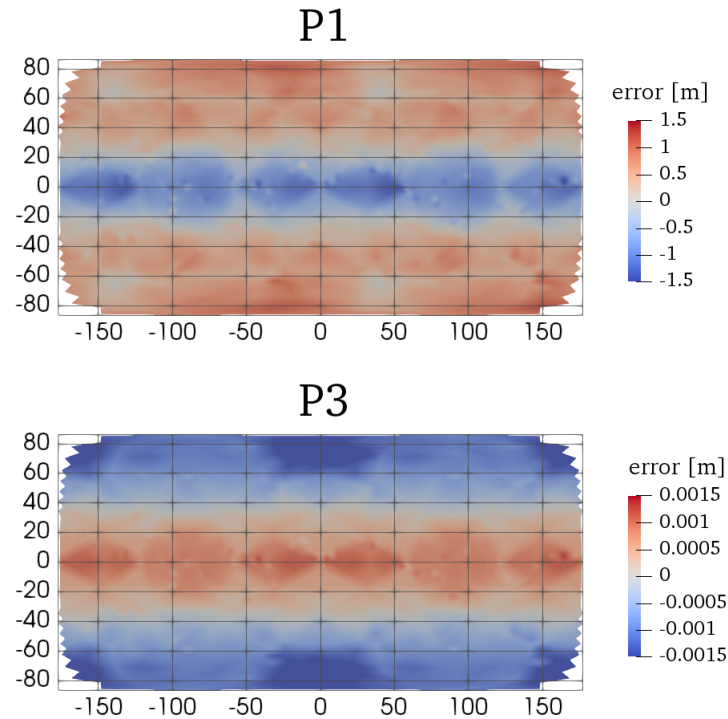


Figure 2: Global Steady-State Nonlinear Zonal Geostrophic Flow. Error plot. Top: P^1 . Bottom: P^3 . Note that color scale change of one order of magnitude for each plot.

grid # ($\alpha = 0$)	$e_1 - P^1$	$e_2 - P^1$	$e_1 - P^2$	$e_2 - P^2$	$e_1 - P^3$	$e_2 - P^3$
1	4.6261e-02	5.1549e-02	2.7469e-03	3.8020e-03	3.4459e-04	4.8972e-04
2	8.5532e-03	9.8352e-03	2.2773e-04	2.9368e-04	1.4836e-05	2.1296e-05
3	1.4574e-03	1.7889e-03	2.2788e-05	2.8277e-05	8.1059e-07	1.0731e-06
4	2.8337e-04	3.6591e-04	2.5750e-06	3.1282e-06	4.7899e-08	6.3057e-08
5	6.2480e-05	8.2598e-05	3.0803e-07	3.7606e-07	2.9741e-09	3.9206e-09
Order	2.3980	2.3319	3.2711	3.3160	4.1919	4.2260

Table 1: Global Steady-State Nonlinear Zonal Geostrophic Flow. L^1, L^2 error norm and convergence rate. The order is computed from a linear fit of the 5 points.

with $b_0 = 2000 m$, $R = \pi/9$, $r^2 = \min(R^2, (\varphi - \varphi_0)^2 + (\lambda - \lambda_0)^2)$ and with the center of the cone in $(\varphi_0, \lambda_0) = (3/2\pi, \pi/6)$. Simulations are performed on the fourth icosahedral grid ($h_K = 446 km$). Figure 3 provides height contour lines for P^1, P^2 and P^3 computations after 15 days of physical time. For this case one typically checks the conservation of total mass and energy

$$E = h \left(\frac{1}{2} \|\mathbf{u}\|^2 + g \frac{h}{2} + gb \right) \quad (57)$$

273 Mass error should be only related to round-off errors. Regarding the energy, the proposed scheme have no
274 provable energy conservation properties, which makes the definition of the actual discrete evaluation of
275 the energy somewhat arbitrary. In practice, here the energy is computed directly from nodal quantities,
276 and then integrated using the high order finite element approximation. After 15 days mass is conserved
277 within a relative error of $1e - 13$. Relative energy conservation error is reported on the right column in
278 figure 3 it is comparable to or better than those typically reported in literature. In the same figure we
279 compare with a second order residual distribution scheme proposed by the authors [32], with a third order
280 FV scheme on a cubed sphere [5] and with the high resolution results by the German Weather Service
281 (DWD) <http://icon.enes.org/swm/stswm/node5.html>.

282 Unstable Jet. The last global test taken from [31] consists of a geostrophically balanced mid-latitude jet,
283 to which a small perturbation is added to initiate the instability. We use this test to confirm that the polar
284 treatment has no impact on the numerical solution and on its derivatives. We look to the vorticity field
285 for P^1, P^2 and P^3 solutions but with two different z_{lim} , the one used in other experiments $z_{lim} = 0.9R$
286 and $z_{lim} = 0.75R$ for which the polar cap interface falls exactly into the jet. Mesh convergence has been
287 carried on two successive icosahedral grids (level 5 and 6, respectively $223 km$ and $111 km$), see figures 4,
288 5. At both mesh level, P^1 solution is insufficient to support the vortex evolutions. Increasing the order,

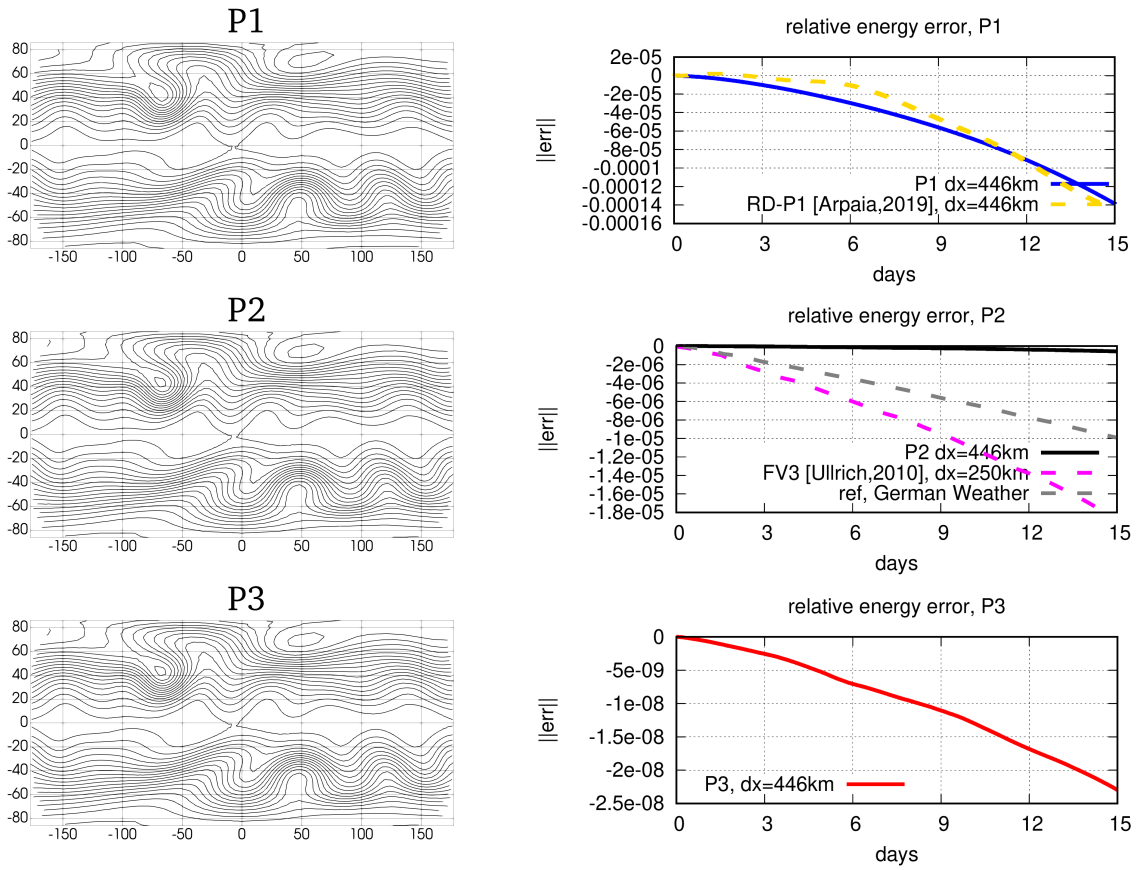


Figure 3: Zonal flow over an isolated mountain. Left: Snapshot at day 15 (depth contour levels from 5050 m to 5950 m -intervals of 50 m). Right: relative energy error (results from [5, 32] and from the DWD reported for comparison where relevant)

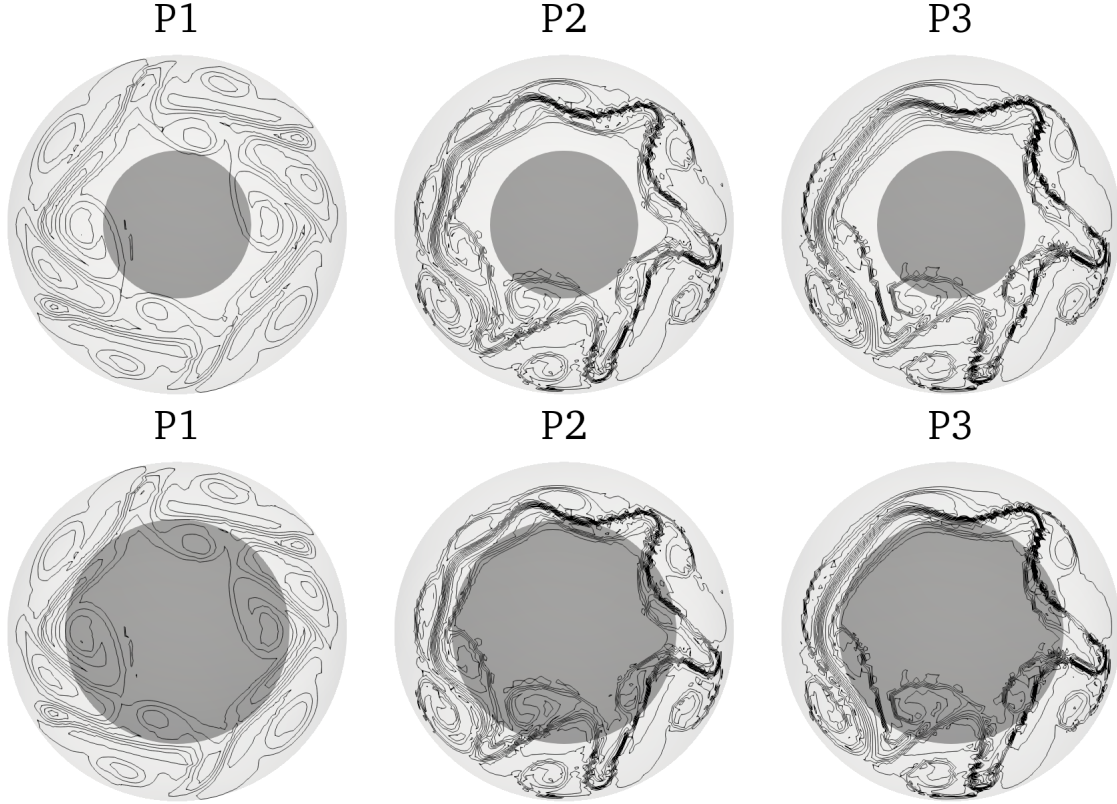


Figure 4: Unstable Jet. Coarse resolution $h_K = 223 \text{ km}$. Dark grey area represents a circle with radius $R\sqrt{1 - (\frac{z_{\text{lim}}}{R})^2}$ (polar cap region). **Top:** $z_{\text{lim}} = 0.9R$. **Bottom:** $z_{\text{lim}} = 0.75R$. Contour levels from $-1.1e - 4$ to $1.5e + 4$.

289 P^2, P^3 computations at mesh level 5 provide the correct dynamics but the vorticity contours are a little
 290 bit jagged. At level 6 much of the jaggedness disappears.

291 **6.2. Small amplitude barotropic waves**

With this test we look to the impact of the well balancing correction for classical oceanic applications such as tidal and surge waves. We have taken a basin spanning from 0° to $25^\circ E$ and from $35^\circ N$ to $55^\circ N$. The bathymetry is a smooth Gaussian hump mimicking a continental shelf and an isolated mountain:

$$b = \max(b_0 \exp\{-r_0^2/R\}, b_1 (1 - r_1/R))$$

with $b_0 = 2000 \text{ m}$, $R_0 = \pi/12$, $r_0^2 = 8.5(\varphi - \varphi_0)^2 + (\lambda - \lambda_0)^2$, $(\varphi_0, \lambda_0) = (0, \pi/4)$ and $b_1 = 4000 \text{ m}$, $R_1 = 5\pi/180$, $r_1^2 = (\varphi - \varphi_1)^2 + (\lambda - \lambda_1)^2$, $(\varphi_1, \lambda_1) = (10\pi/180, 48\pi/180)$. The mesh is an unstructured triangulation with topology shown in the top of figure [\(6\)](#) and constant mesh size $h_K = 100 \text{ km}$. For a

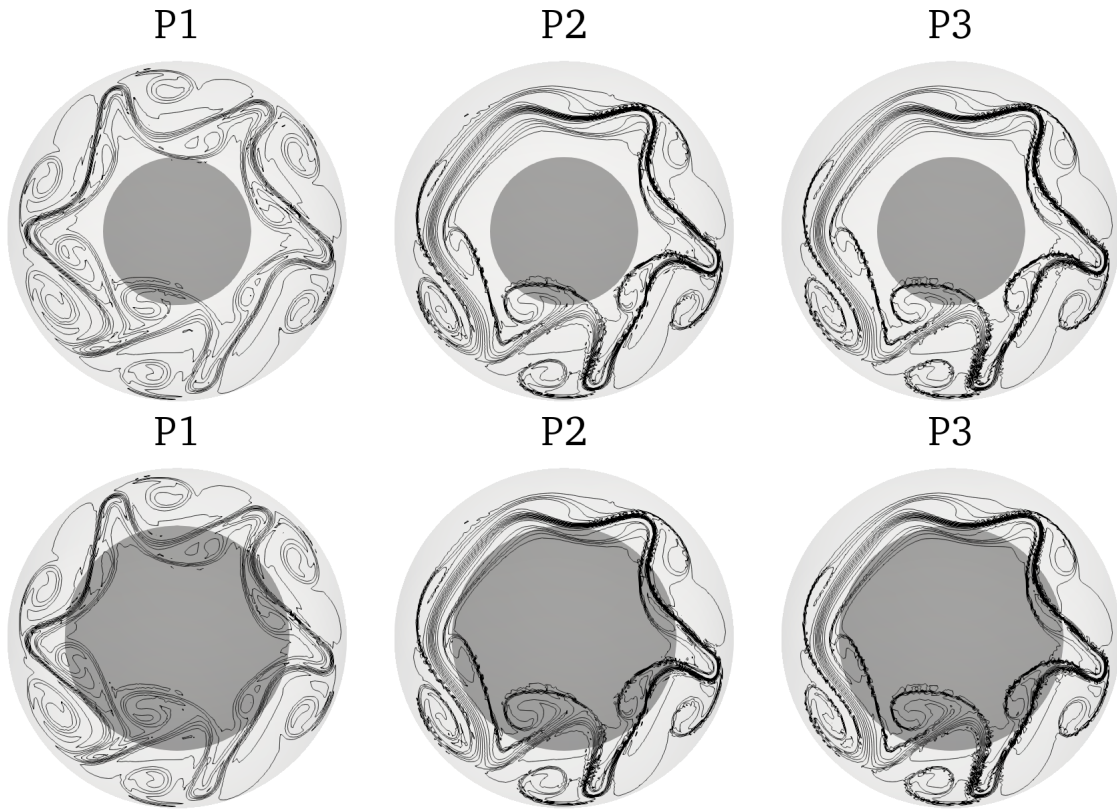


Figure 5: Unstable Jet. Fine resolution $h_K = 111 \text{ km}$. Dark grey area represents a circle with radius $R\sqrt{1 - (\frac{z_{\text{lim}}}{R})^2}$ (polar cap region). **Top:** $z_{\text{lim}} = 0.9R$. **Bottom:** $z_{\text{lim}} = 0.75R$. Contour levels from $-1.1e - 4$ to $1.5e + 4$.

lake at rest state with initial level $\eta_0 = 5000\text{ m}$ the well balanced spherical formulation (43) exhibits a maximum perturbation of the velocity norm in the range $1e - 12$ to $1e - 13$ depending on the polynomial order. After this well balancing test, a small amplitude tidal signal $\eta_0 + A \sin(\frac{2\pi}{T}t)$ is imposed at the north boundary ($A = 0.01\text{ m}$, $T = 12.42\text{ hrs}$). The eastern boundary is a wall to let a southward propagating barotropic Kelvin wave develop. We compare (43) against the non well balanced scheme based on the weak formulation (32). In the left block of figure (6) two snapshots of upwelling/downwelling at the lateral wall show that the P1 solution of the non well balanced scheme is affected by small wiggles. The perturbation tend to disappear, as expected, with mesh resolution (see right block) and with polynomial order (not shown). A second test has been carried by forcing a surge wave with a small amplitude atmospheric depression:

$$p_{atm}(\varphi, \lambda, t) = p_0 - \Delta p \exp\left(\frac{r(\varphi, \lambda, t)}{\sigma^2}\right)$$

with r the distance from the center of the storm which is translating southward at constant speed U . The parameters are set to $p_0 = 101\text{ kPa}$, $\Delta p = 0.3\text{ kPa}$, $\sigma = 350\text{ km}$ and $U = \sqrt{100g}$. In figure (7) we show the impact of the well balanced correction. Again, at the coarse resolution (left block), the small-amplitude gravity waves that propagates faster then the storm are much wiggled in the non well balanced case. Increasing mesh resolution (see right block) and polynomial order (not shown) makes again such wiggles negligible.

6.3. Circular hump centered at the equator

This is a test proposed in (6). The initial condition is a circular depth disturbance at the equator:

$$h(\varphi, \lambda) = \begin{cases} 2 & \text{if } \arccos(\cos \varphi \cos \lambda) \leq 0.2 \\ 0.2 & \text{otherwise} \end{cases}, \quad \mathbf{u}(\varphi, \lambda) = 0 \quad (58)$$

This initial condition is symmetric about the point $(\varphi, \lambda) = (0^\circ, 0^\circ)$, and should remain symmetric in absence of rotation. Shock capturing is necessary to well represent the discontinuity. We run computations on two half sphere meshes generated with `gmsh`: a coarse one with 2436 points; a fine one with 9187 points. In figure (8) we compare the solution contours obtained with P1/P2 on the coarse mesh against a P1 solution on the fine mesh. We observe mesh/order convergence for this non-smooth case. At $t = 0.9$ the P2 solution on the coarse mesh is of the same order of accuracy of the P1 solution on the fine mesh.

We repeat the same test adding rotation effects. We set the dimensionless rotation rate to $\Omega = 5$. In figure (9) we report depth contour lines at $t = 1.2$. As in the previous case, we observe the higher resolution obtained with P2 scheme both in smooth and discontinuous regions.

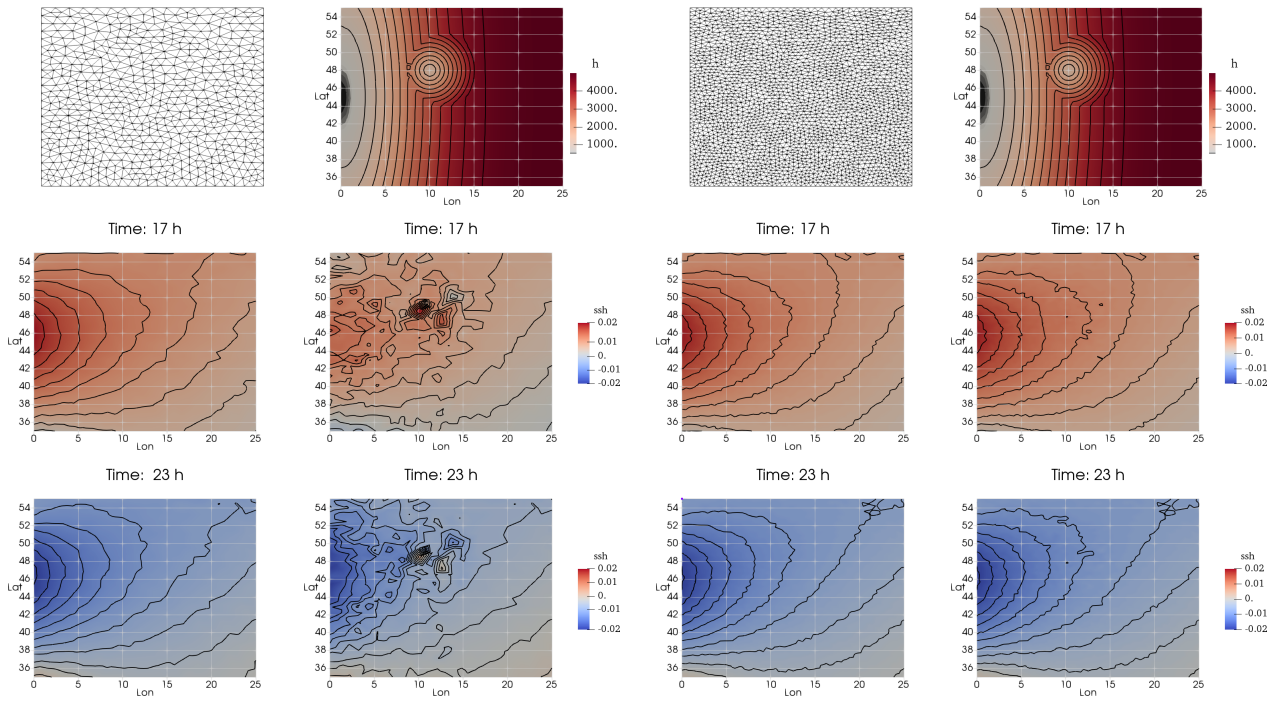


Figure 6: Small amplitude tidal wave. Coarse $h_K = 100 \text{ km}$ (left block) and fine $h_K = 50 \text{ km}$ (right block) simulation. Top: mesh and bathymetry. Middle and bottom: snapshot of the free surface at $t = 18h$ and $23h$. Left: well balanced scheme. Right: non well balanced scheme. Contour levels are from -0.02 m to 0.02 m in intervals of 0.002 m .

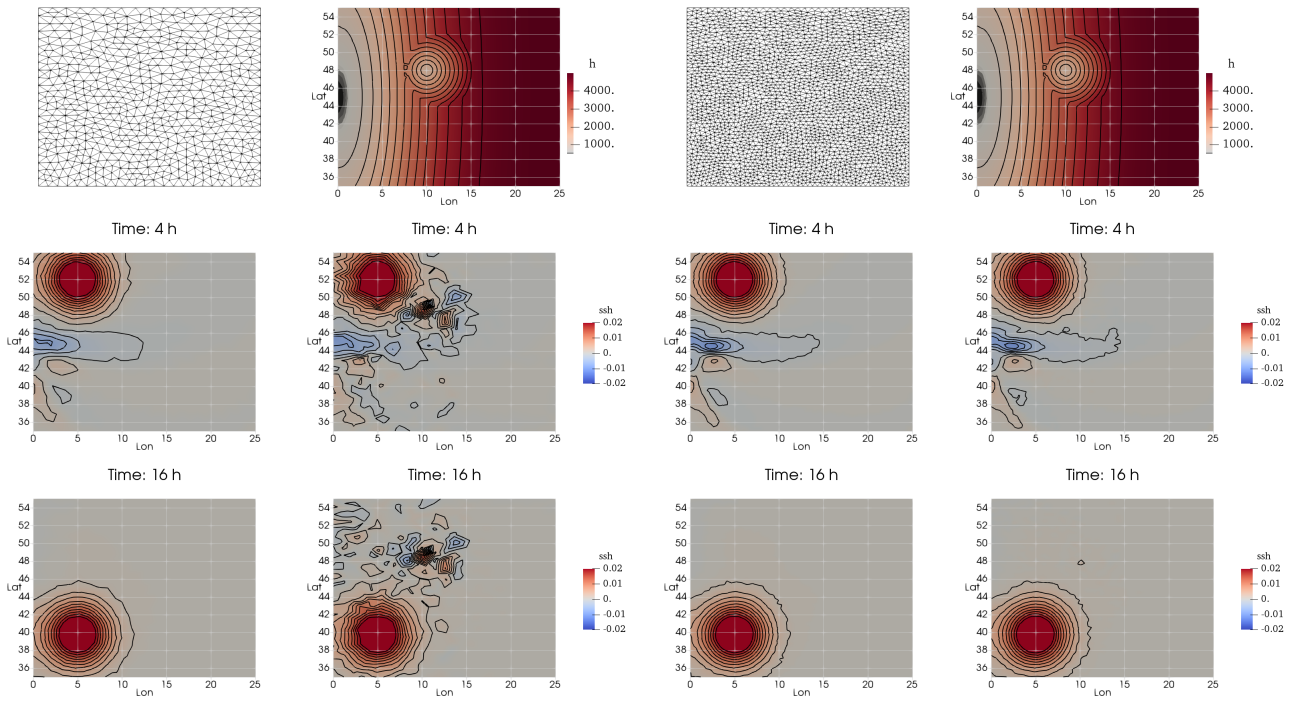


Figure 7: Small amplitude surge wave. Coarse $h_K = 100 \text{ km}$ (left block) and fine $h_K = 50 \text{ km}$ (right block) simulation. Top: mesh and bathymetry. Middle and bottom: snapshot of the free surface at $t = 4h$ and $16h$. Left: well balanced scheme. Right: non well balanced scheme. Contour levels are from -0.02 m to 0.02 m in intervals of 0.002 m .

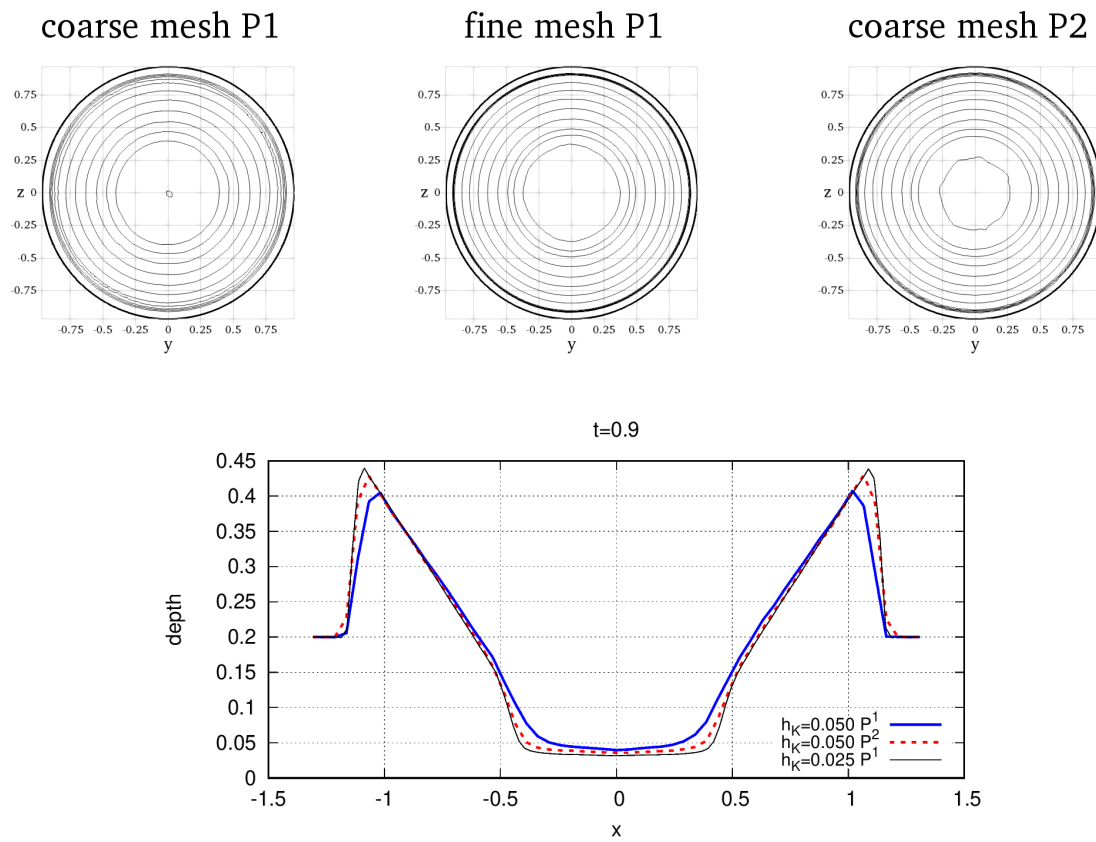


Figure 8: Circular Hump. Contour levels at $t = 0.9$ from 0.04 m to 0.5 m in intervals of 0.045 m . Bottom: cut along the equator

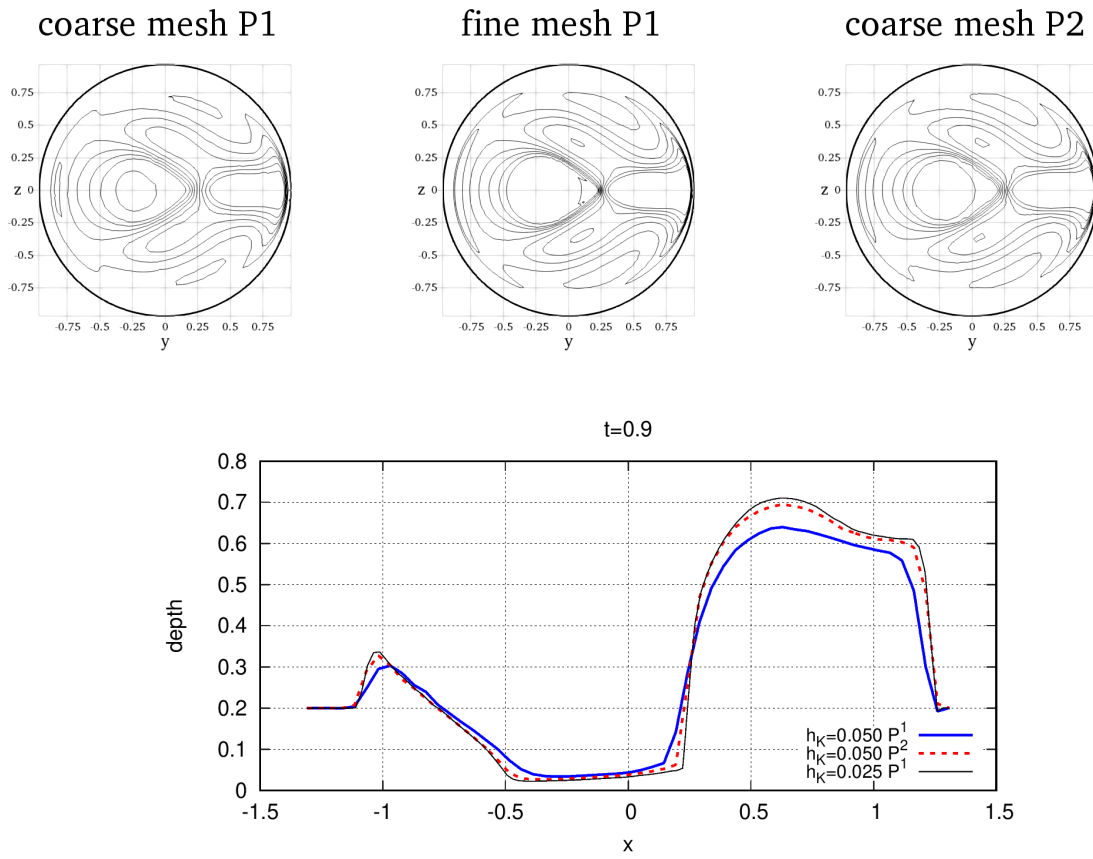


Figure 9: Circular Hump with rotation. Contour levels at $t = 1.2$ from 0.04 m to 0.5 m in intervals of 0.045 m . Bottom: cut along the equator

309 *6.4. Realistic external gravity waves simulations*

310 Finally, to show the potential of this method, we perform two realistic simulations in the Caribbean Sea.
311 The computational domain, the bathymetry and the mesh were specified by the consortium of the project
312 Interreg Carib-Coast (<https://www.interreg-caraibes.fr/carib-coast>). The domain in figure [10](#) spans from
313 $50^\circ W$ to $84.7^\circ W$ and from $8.4^\circ N$ to $22.1^\circ N$. The bathymetry at the degrees of freedom is computed from
314 GEBCO (www.gebco.net) and from SHOM for the French west indies (<https://data.shom.fr/donnees>).
315 Land boundaries are treated as reflective walls. To avoid wetting/drying of cells near the coastline, we have
316 filtered the bathymetry at land masses contained in the computational domain with $b_{filt} = \min(b, -1)$.
317 The filter assures that all the cells are always wet, avoiding positivity preserving issues and well balancing of
318 partly dry cells, all aspects not addressed in the present study. The mesh has variable mesh size ranging
319 from $h_{K,max}$ in deep ocean to $h_{K,min}$ at the coast in correspondence of Martinique, Guadeloupe and
320 Saint Martin islands, which represent some interest sites of the Carib-Coast project. A fine and a coarse
321 mesh have been generated, respectively with $h_{K,min} = 300 m$, $h_{K,max} = 10 km$ and $h_{K,min} = 600 m$,
322 $h_{K,max} = 20 km$. The Manning friction term is set to $n = 0.025$ for this case.

323 *6.4.1. Tsunami in Carribean Sea*

324 The initial tsunami waveform is associated with a random rupture of the Lesser Antilles subduction
325 zone. We use the fault configuration proposed by Feuillet et al. characterized by a magnitude $M_w = 8.4$
326 (for the fault parameters see [33](#)). Randomness is associated to the heterogeneity of the fault slip which
327 is computed by a Karuhnen-Loeve expansion [34](#). Then, the initial waveform is the solution of the Okada
328 linear model. We have equipped the domain with several gauges placed in the near and far-field. In the
329 near-field we distinguish coastal gauges in bays or harbours (Point-a-Pitre, Fort-de-France) and nearshore
330 gauges on the continental shelf (Martinique NE, Martinique W). At far-field we have placed the gauges
331 in the Carribean sea (Kingston) and close to east boundary (Atlantic) in order to look both to tsunami
332 propagation after the wave has passed the Antillean Arch and free propagation in deep ocean. In figure
333 [12](#) we report the sea surface height recorded at the gauge stations for P1/P2 simulations on the coarse
334 mesh and we compare them with the P1 simulation on the fine mesh. The coarse P2 solution has roughly
335 the same accuracy of the fine P1 solution in the near-field and it is superior for far-field propagation. For
336 the near-field gauges the P1 solution captures sufficiently well the incoming, trapped and reflected wave
337 train, even if the leading wave peak is slightly underestimated with respect to P2 (40 cm at Point-a-Pitre).
338 For far-field gauges P1 solution is very diffusive, probably due to the simple Lax-Friedrich flux employed
339 in this study. Similar results emerge from the snapshot of the sea surface height at $t = 5400 s$ [11](#). In

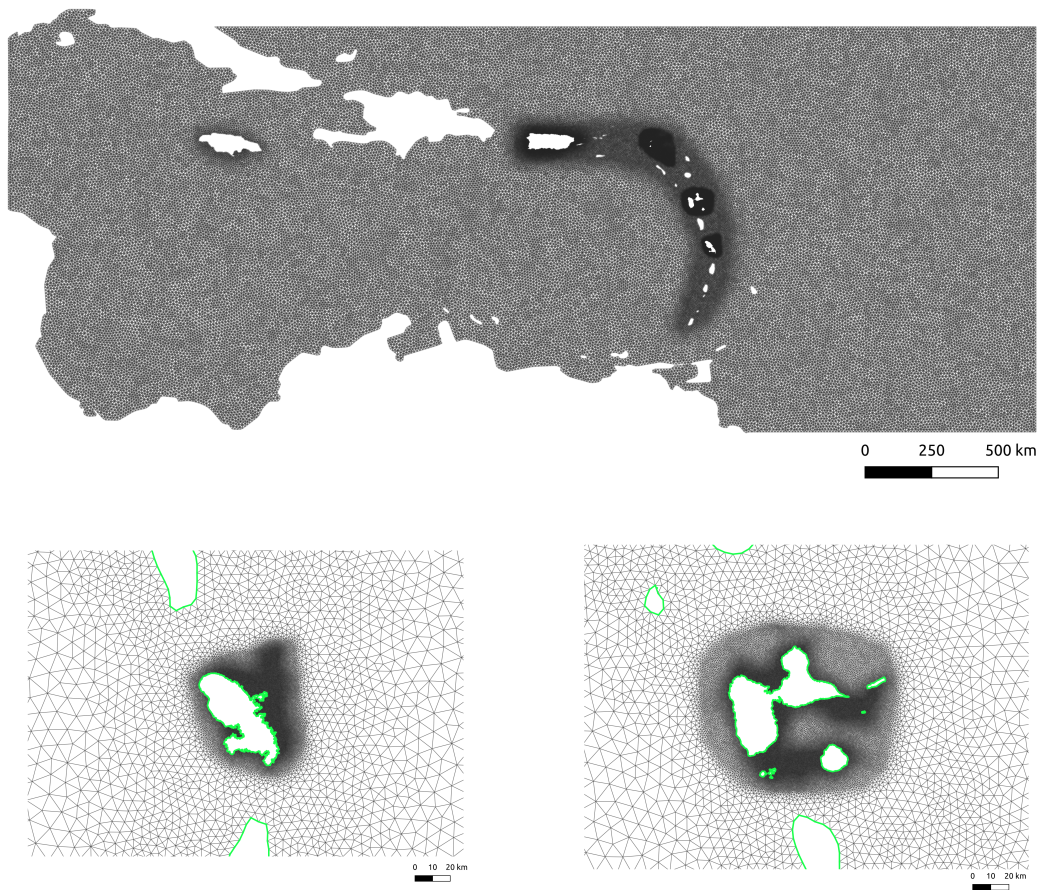


Figure 10: Realistic simulations in Caribbean Sea. Top: Full fine mesh. Bottom: Zoom of the fine mesh in correspondence of Martinique and Guadalupe island.

340 figure [12](#), beyond mesh and order convergence we have validated the simulation against the structured
 341 high order FV code FUNWAVE-TVD [35](#) on a regular grid with $\Delta x = 800 m$ (which has roughly the same
 342 degrees of freedom of the P2 coarse simulation). The comparison is valid for the first two hours (after
 343 FUNWAVE-TVD solution is polluted by wave reflection from the boundary, see the gauge Atlantic Ocean
 344 close the western boundary).

345 6.4.2. *Irma hurricane*

We perform the simulation of the atmospheric surge produced by the passage of hurricane Irma in the Caribbean sea (from 30th August 2017 to 14th September 2017). As known, such phenomena link up great depressions and strong winds, leading to sea level rise and flooding risk at the coast. In order to account for atmospheric forcing, the source term of the shallow water equations has to be modified as shown in [3](#), with the wind force f_w defined by:

$$f_w = c_D \frac{\rho_{air}}{\rho_0} |\mathbf{u}_{10}| \mathbf{u}_{10} \quad (59)$$

346 where ρ_{air} is the air density, \mathbf{u}_{10} is the wind velocity field ten meters above the ground and c_D is the
 347 wind stress coefficient as proposed by Charnock [36](#) with Charnock parameter set to 0.022 [37](#). To
 348 construct the hurricane pressure and wind fields, we used information issued from the NOAA IBTRACKS
 349 [38](#) database and we applied the Holland parametric model [39](#). Computed hurricane winds are, then,
 350 converted to surface winds and averaged over 10 minutes. After that, cyclonic wind and pressure fields are
 351 finally merged with data from CFSR model [40](#) in order to represent large-scale atmospheric conditions in
 352 the whole computational domain. Our simulations run from 05th September 2017 to 08th September 2017,
 353 simulating the hurricane strike on Caribbean French islands, Virgin islands and Puerto Rico. Figure [13](#)
 354 shows the hurricane surge propagation, simulated by the P1 coarse mesh. Indistinguishable results, at this
 355 scale, are obtained using the P2 coarse mesh, thus they are not reported here. Several NOAA/NOS and
 356 SHOM tide-gauges are available in the area, allowing to validate our simulations against real observations.
 357 Measured sea level is the result of several components: the tide, a seasonal adjustment due to baroclinicity
 358 [41](#), the setup due to breaking waves and, finally, the atmospheric surge due to wind and pressure. The first
 359 three components cannot be reproduced by our model. Therefore, before comparison, we processed raw
 360 signals such as to remove the tide and we applied a mean sea level offset to account for baroclinicity [42](#).
 361 In this way, we were able to produce the pictures of figure [14](#), comparing simulations and observations at
 362 four gauges located close to the hurricane track. We can appreciate a global agreement between computed
 363 water levels by both P1 and P2 simulations and historical data. The use of P2 approximations, in this
 364 case, leads to very few improvements in the results, only noticeable on the pick representation at the

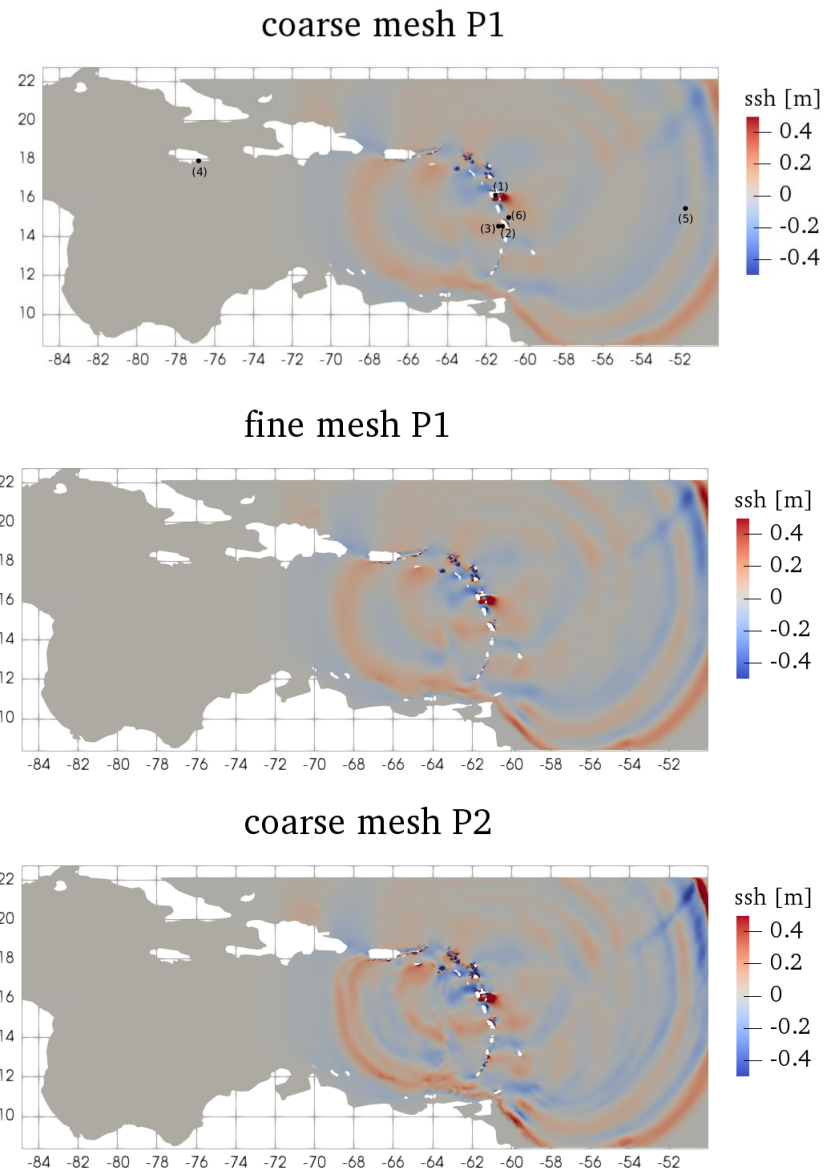


Figure 11: Tsunami in the Carribbean Sea. Color map of sea surface height η after 5400 s. Numbers (1) to (6) in the top picture show the position of the six stations considered in Figure 12 which corresponds to: (1) Pointe-a-Pitre, (2) Fort-de-France, (3) Martinique W, (4) Kingston, (5) Atlantic Ocean, (6) Martinique NE.

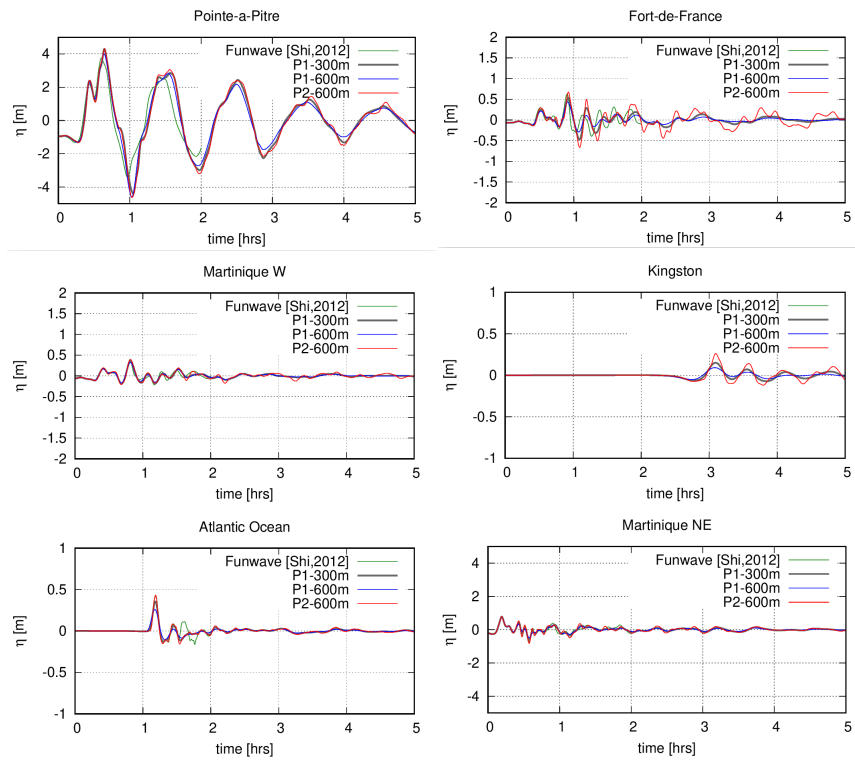


Figure 12: Tsunami in the Carribean Sea. Water height recorded at the gauge stations located at Point-a-Pitre (top-left), Fort-de-France (top-right), Martinique W (middle-left), Kingston (middle-right), Atlantic Ocean (bottom-left) and Martinique NE (bottom-right)

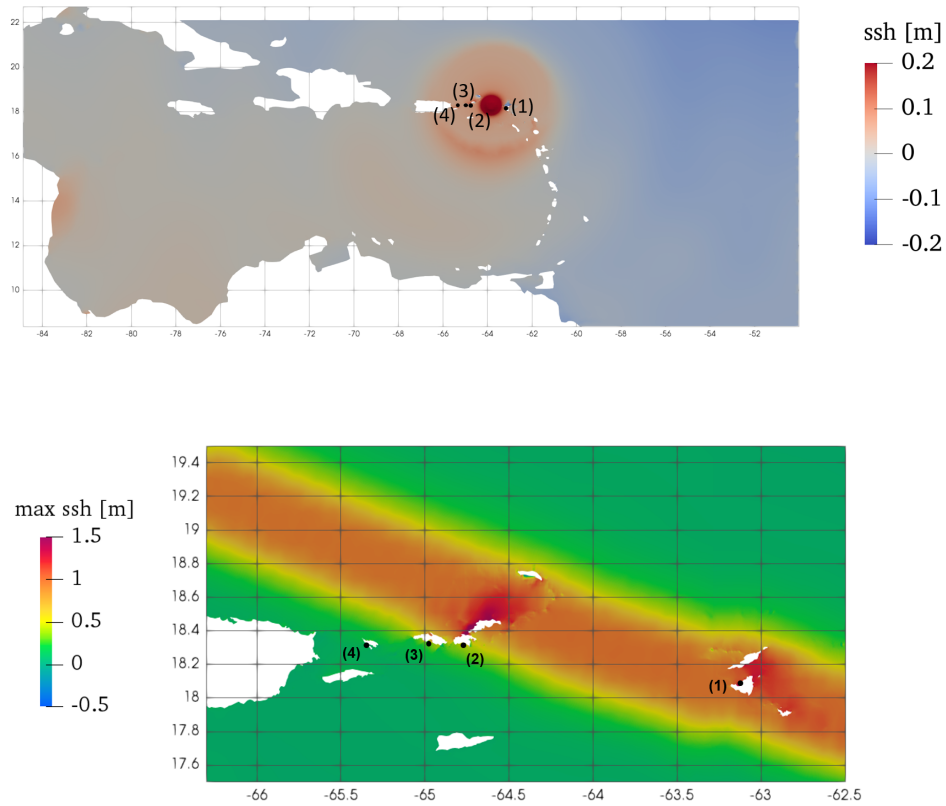


Figure 13: Hurricane Irma. Top: color map of the simulated surge the 06/09/2017 14:00:00. Bottom: close up view of the maximum water surface elevation in the region of Puerto Rico. Numbers (1) to (4) show the position of the four stations considered in Figure 14 which respectively corresponds to: (1) Saint Martin, (2) Lameshur Bay, (3) Charlotte Amalie, (4) Culebra locations.

365 location closest to the hurricane track: Saint Martin and Lameshur. Discrepancies in the results may be
 366 due to different factors, such as the parametric reconstruction of hurricane pressure and wind fields. Other
 367 source of discrepancies may be due to the wave setup contribution to observed water level, and/or the
 368 coarse representation of the insular shelf ($> 1km$) in the computational mesh of the Carib-Coast project.
 369 Further investigations could improved the results, but this is beyond the purposes of this work and they
 370 are not performed here.

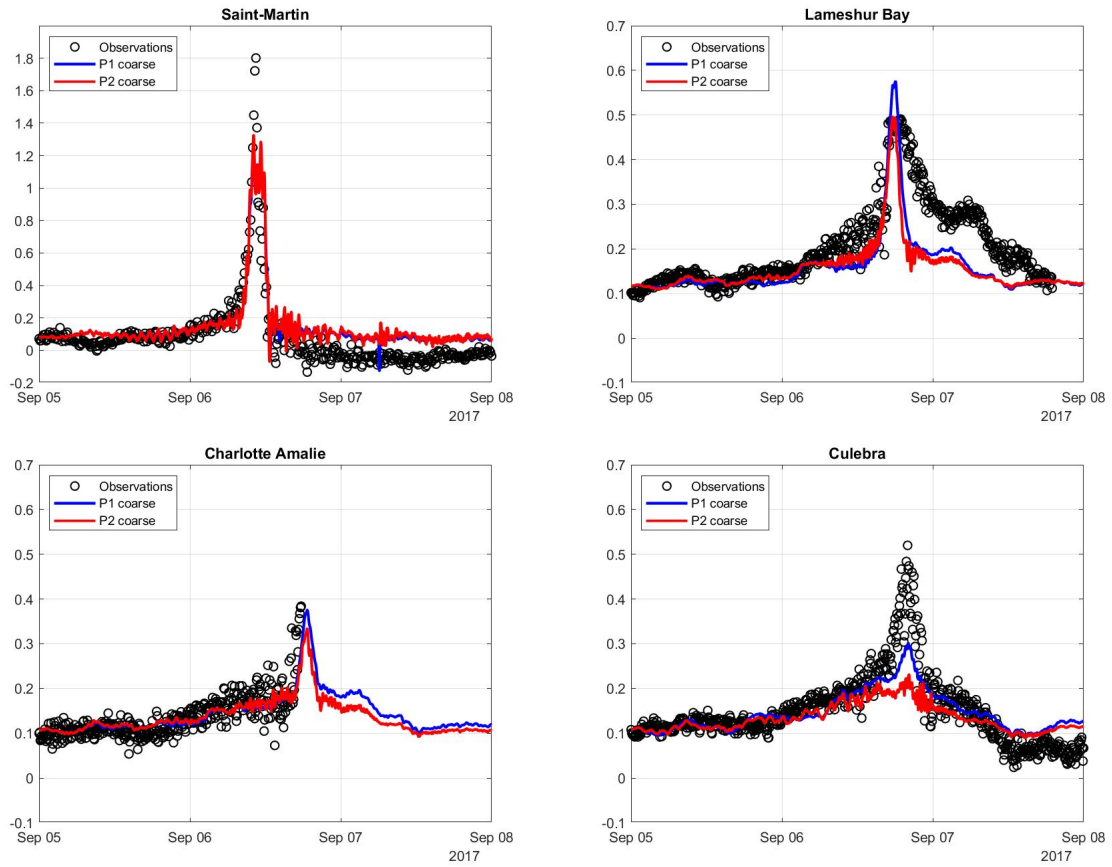


Figure 14: Hurricane Irma. Comparison of simulated sea surface height signals (scale in meters) at a selection of gauge stations, located at Saint Martin (top-left), Lamashur Bay (top-right), Charlotte Amalie (bottom-left) and Culebra (bottom-right).

371 7. Conclusion

372 In this work we have discussed an efficient and accurate formulation of the spherical Shallow Wa-
373 ter equations in the form originally proposed in [10] which implies a mixed 3d/2d treatment: the time
374 derivative is expressed in 2d form while the right hand side is formulated in 3d Cartesian form. We have
375 shown that using, for the 2d part, covariant vector basis, the implementation simplifies and the accu-
376 racy increases. In this work we have opted for a Discontinuous Galerkin discretization but the mixed
377 3d/2d-covariant form is in principle also more amenable to a continuous Finite Elements discretization
378 w.r.t to the original [10]. In particular local mass matrix goes back to the standard block-diagonal form,
379 line integrals or Riemann Problem do not imply tensor/vector rotation thanks to the continuity of the
380 normals at the edges. We have also discussed a well balanced form of the resulting DG scheme resorting
381 the hydrostatic pressure term to the strong form. Finally with a realistic tsunami and an historical storm
382 surge simulation we have validated the method for two different oceanographic applications.

383 Ongoing work is devoted to extension of the discretization of the 3d/2d-covariant Shallow Water
384 equations to stabilized continuous Finite Element (SUPG or Continuous Interior Penalty see e.g. [15, 43]
385 and references therein), and to perform a one to one comparison with the current implementation.

386 **Appendix: Bounds on the integration by parts correction**

387 To prove the bounds (41) we start by characterizing the mapping (12) used for the quadrature with a
 388 classical property (see e.g. [44, 45] for curved finite element examples).

389

390 **Property 1.** (Bounds on the mapping derivatives) *The mapping (12) and its derivatives verify the*
 391 *following estimates:*

$$\mathbf{J}_A = \mathcal{O}(h) \tag{60}$$

$$\nabla_{\mathbf{X}}^m \mathbf{J}_A = \mathcal{O}(h^{m+1}) \tag{61}$$

$$J_A = \mathcal{O}(h^2) \tag{62}$$

$$\nabla_{\mathbf{X}} J_A = \mathcal{O}(h^3) \tag{63}$$

Proof. To prove the estimates we start by noting that, denoting by $\mathbf{x}_G = \sum_{j=1}^3 \mathbf{x}_j/3$

$$F^l(\mathbf{X}) = \sum_{j=1}^3 \varphi_j(\mathbf{X}) x_j^l = x_G^l + \sum_{j=1}^3 \varphi_j(\mathbf{X})(x_j^l - x_G^l) := x_G^l + h \sum_{j=1}^3 \delta_j^l \varphi_j(\mathbf{X})$$

with $\delta_j^l = (x_j^l - x_G^l)/h$ the rescaled components of the distance of the nodal positions from the average, which is of $\mathcal{O}(1)$ for shape regular meshes, and with φ_j the linear finite element basis. The above expression can be written as a linear multivariate polynomial in terms of the components of $h\mathbf{X}$, with $\mathcal{O}(1)$ coefficients. We write succinctly

$$F^l = p_l^1(h\mathbf{X}) \tag{64}$$

and similarly

$$x^l(\mathbf{X}) = \frac{p_l^1(h\mathbf{X})}{\|F\|}$$

where now with $p^k(h\mathbf{X})$ we denote a multivariate polynomial of degree k in the components of $h\mathbf{X}$, with $\mathcal{O}(1)$ coefficients. To obtain the first two estimates we prove that any k^{th} order differential of the mapping (w.r.t. any component or combination of the components of \mathbf{X}) verifies

$$\partial^k x^l(\mathbf{X}) = h^k \frac{p_l^{k+1}(h\mathbf{X})}{\|F\|^{2k+1}}. \tag{65}$$

To prove by induction we check the initial condition:

$$\partial x^l(\mathbf{X}) = \frac{\|F\| \partial p_l^1(h\mathbf{X}) - p_l^1(h\mathbf{X}) \partial \|F\|}{\|F\|^2}$$

We can use now [\(7\)](#) to write

$$\partial\|F\| = \frac{h}{\|F\|} \sum_{m=1}^3 \sum_{j=1}^3 F^m(\mathbf{X}) \delta_j^m \partial\varphi_j(\mathbf{X})$$

where note that the derivatives of the linear basis functions are of $\mathcal{O}(1)$, in particular, they assume the values 1, 0 or -1 on the standard unit triangle containing the origin of the parametric space. We can write

$$\partial x^l(\mathbf{X}) = \frac{\|F\|^2 \partial p_l^1(\mathbf{h}\mathbf{X}) - h p_l^1(\mathbf{h}\mathbf{X}) \sum_{m=1}^3 \sum_{j=1}^3 F^m(\mathbf{X}) \delta_j^m \partial\varphi_j(\mathbf{X})}{\|F\|^3}$$

All it remains is to note that the derivative of $p_l^1(\mathbf{h}\mathbf{X})$ can be written as $a_{0l}h$ for some $\mathcal{O}(1)$ constant a_{0l} , so that

$$\partial x^l(\mathbf{X}) = h \frac{\|F\|^2 a_{0l} - p_l^1(\mathbf{h}\mathbf{X}) \sum_{l=1}^3 \sum_{j=1}^3 F^l(\mathbf{X}) \delta_j^l \partial\varphi_j(\mathbf{X})}{\|F\|^3}$$

in which the numerator is indeed a quadratic polynomial of the components of F , which combined with [\(64\)](#) leads to

$$\partial x^l(\mathbf{X}) = h \frac{p_l^2(\mathbf{h}\mathbf{X})}{\|F\|^3}.$$

We need now to prove that, if true for $k-1$, the statement is also true for k , so we assume that

$$\partial^{k-1} x^l(\mathbf{X}) = h^{k-1} \frac{p_l^k(\mathbf{h}\mathbf{X})}{\|F\|^{2k-1}}$$

and compute its differential:

$$\begin{aligned} \partial^k x^l(\mathbf{X}) &= h^{k-1} \frac{\partial p_l^k(\mathbf{h}\mathbf{X}) \|F\|^{2k-1} - p_l^k(\mathbf{h}\mathbf{X}) (2k-1) \|F\|^{2k-2} \partial\|F\|}{\|F\|^{4k-2}} = h^{k-1} \frac{\partial p_l^k(\mathbf{h}\mathbf{X}) \|F\|^2 - p_l^k(\mathbf{h}\mathbf{X}) (2k-1) \|F\| \partial\|F\|}{\|F\|^{4k-2-(2k-3)}} \\ &= h^{k-1} \frac{\partial p_l^k(\mathbf{h}\mathbf{X}) \|F\|^2 - h p_l^k(\mathbf{h}\mathbf{X}) (2k-1) \sum_{l=1}^3 \sum_{j=1}^3 F^l(\mathbf{X}) \delta_j^l \partial\varphi_j}{\|F\|^{2k+1}} \end{aligned}$$

As before, we remark that $\partial p_l^k(\mathbf{h}\mathbf{X}) = h \bar{p}_l^{k-1}(\mathbf{h}\mathbf{X})$, which allows to write

$$\partial^k x^l(\mathbf{X}) = h^k \frac{\bar{p}_l^{k-1}(\mathbf{h}\mathbf{X}) \|F\|^2 - h p_l^k(\mathbf{h}\mathbf{X}) (k+1) \sum_{l=1}^3 \sum_{j=1}^3 F^l(\mathbf{X}) \delta_j^l \partial\varphi_j}{\|F\|^{2k+1}}$$

392 which indeed by virtue of [\(64\)](#) can be written as [\(65\)](#), and concludes the induction.

To conclude this preliminary proof, we note that given an upper bound to the mesh size $H > h$, we can easily find a uniformly bounded constant C_H such that $\|F\|$ is bounded in between R and $R - C_H H$ and $1/\|F\|$ is bounded as well. Using this remark, and the boundedness and the coefficients of p_l^k , the

first of the properties sought is obtained for $k = 1$, the second for $k = m + 1$. The $k = 1$ property allows readily to prove (62) by using the definition

$$J_A = \sqrt{G}, \quad G = \det(\mathbf{J}_A^t \mathbf{J}_A)$$

393 Since the determinant of a 2×2 matrix is a quadratic form of the matrix entries, this means that $G = \mathcal{O}(h^4)$
 394 by virtue of (60) and $\sqrt{G} = \mathcal{O}(h^2)$, which implies (62) by the definition of J_A . Lastly the properties (60)-
 395 (61)-(62) can be used to show that $\nabla_{\mathbf{X}} J_A = \mathcal{O}(h^3)$, hence (63). \square

396

To complete the proof of the estimate, we now rewrite each of the integrals in the parametric space, and perform a truncated Taylor series expansion with the appropriate degree in the parametric coordinates to obtain an estimate of the quadrature error. We will show the procedure for one of the integrals of (40), and provide comments concerning possible differences when evaluating others. So, let us consider the evaluation of

$$\mathcal{I}_1 = \int_{\mathcal{K}} (P_h \mathbf{I}) : \varphi_i \nabla \mathbf{g}_\alpha^* d\mathbf{x} \quad (66)$$

As we said in the main body of the paper \mathbf{g}_α^* is available in a uniformly bounded analytical form, for example in latitude-longitude coordinates. Note that, with the usual assumption of smoothness, removing from the variational form its analog evaluated on an exact regular solution would lead to estimating the last integral via expressions of the type

$$\int_{\mathcal{K}} ((P_h^{ex} - P^{ex}) \mathbf{I}) : \varphi_i \nabla \mathbf{g}_\alpha^* d\mathbf{x}$$

397 which provide at best an estimate of an $\mathcal{O}(h^{p+3})$, which is related to the approximation error, and it
 398 is independent on the quadrature. However the theoretical and numerical evidence indicates a stricter
 399 bound, as we will show shortly.

First we write the integral in the parametric space:

$$\mathcal{I}_1 = \int_K (P_h(\mathbf{x}(\mathbf{X})) \mathbf{I}) \varphi_i(\mathbf{X}) \nabla \mathbf{g}_\alpha^*(\mathbf{x}(\mathbf{X})) J_A(\mathbf{X}) d\mathbf{X}$$

The above integral can be written regrouping the terms as

$$\mathcal{I}_1 = \int_K \hat{f}(\mathbf{X}) \mathcal{J}_{iA}(\mathbf{X}) d\mathbf{X}$$

having separated for convenience the terms that are defined directly in the reference space $\mathcal{J}_{iA}(\mathbf{X}) = \varphi_i(\mathbf{X}) J_A(\mathbf{X})$ from the terms defined in the physical space $\hat{f}(\mathbf{X}) = f(\mathbf{x}(\mathbf{X}))$. We remark now that we

can write, within each parametric element, \mathcal{J}_{iA} as a 0^{th} order truncated Taylor series:

$$\mathcal{J}_{iA} = \mathcal{J}_{iA}(\mathbf{X}^*) + \nabla_{\mathbf{X}} \mathcal{J}_{iA}(\mathbf{X}_{\mathbf{X}}^{**}) \cdot (\mathbf{X} - \mathbf{X}^*)$$

where, following the Lagrange representation of the Taylor series remainder, for a given \mathbf{X} , the point $\mathbf{X}_{\mathbf{X}}^{**}$ lies along the segment $(\mathbf{X}^*, \mathbf{X})$. We can easily estimate the remainder from

$$\nabla_{\mathbf{X}} \mathcal{J}_{iA}(\mathbf{X}_{\mathbf{X}}^{**}) \cdot (\mathbf{X} - \mathbf{X}^*) = \varphi_i(\mathbf{X}_{\mathbf{X}}^{**}) \nabla_{\mathbf{X}} J_A(\mathbf{X}_{\mathbf{X}}^{**}) \cdot (\mathbf{X} - \mathbf{X}^*) + \nabla_{\mathbf{X}} \varphi_i \cdot J_A(\mathbf{X}_{\mathbf{X}}^{**})(\mathbf{X} - \mathbf{X}^*)$$

400 with $\nabla_{\mathbf{X}} \varphi_i$ constant and of $\mathcal{O}(1)$ in the P^1 case as already remarked. From [\(63\)](#) $\nabla_{\mathbf{X}} J_A(\mathbf{X}_{\mathbf{X}}^{**}) = \mathcal{O}(h^3)$
 401 and $J_A(\mathbf{X}_{\mathbf{X}}^{**}) = \mathcal{O}(h^2)$. It follows that the second term of the above expression is not of higher order so
 402 the rest of the truncated series is of $\mathcal{O}(h^3)$.

We now also develop \hat{f} in a Taylor series truncated at the degree $k_{\mathcal{K}}$ which is the assumed polynomial exactness of the volume quadrature formula. Combining with the previous development, we obtain using standard multi-index notation and again a Lagrange representation of the Taylor series remainder:

$$\begin{aligned} \mathcal{I}_1 = & \int_K \sum_{|\alpha|=0}^{k_{\mathcal{K}}} \frac{1}{\alpha!} D_{\mathbf{X}}^{\alpha} \hat{f}^*(\mathbf{X} - \mathbf{X}^*)^{\alpha} \mathcal{J}_{iA}(\mathbf{X}^*) d\mathbf{X} + \int_K \sum_{|\alpha|=0}^{k_{\mathcal{K}}-1} \frac{1}{\alpha!} D_{\mathbf{X}}^{\alpha} \hat{f}^*(\mathbf{X} - \mathbf{X}^*)^{\alpha} \nabla_{\mathbf{X}} \mathcal{J}_{iA}^{**} \cdot (\mathbf{X} - \mathbf{X}^*) d\mathbf{X} \\ & + \int_K \sum_{|\alpha|=k_{\mathcal{K}}+1} \frac{1}{\alpha!} D_{\mathbf{X}}^{\alpha} \hat{f}^{**}(\mathbf{X} - \mathbf{X}^*)^{\alpha} \mathcal{J}_{iA}(\mathbf{X}^*) d\mathbf{X} + \int_K \sum_{|\alpha|=k_{\mathcal{K}}} \frac{1}{\alpha!} D_{\mathbf{X}}^{\alpha} \hat{f}^{**}(\mathbf{X} - \mathbf{X}^*)^{\alpha} \nabla_{\mathbf{X}} \mathcal{J}_{iA}^{**} \cdot (\mathbf{X} - \mathbf{X}^*) d\mathbf{X} \end{aligned}$$

where we recall that in multi-index notation $D_{\mathbf{X}}^{\alpha} = \frac{\partial^{|\alpha|}}{\partial X_1^{\alpha_1} \partial X_2^{\alpha_2}}$. For brevity we have omitted the explicit dependence of the remainder terms on the $\mathbf{X}_{\mathbf{X}}^{**}$ point (which in principle is different for the two development considered), since it has no relevance in the following. By classical arguments, we claim now that the first two integrals, involving degree $k_{\mathcal{K}}$ polynomials, represent the value obtained with the approximate formula used in our method, so that the remaining terms provide an estimate of the quadrature error:

$$\mathcal{E}_{\mathcal{I}_1} := \int_K \sum_{|\alpha|=k_{\mathcal{K}}+1} \frac{1}{\alpha!} D_{\mathbf{X}}^{\alpha} \hat{f}^{**}(\mathbf{X} - \mathbf{X}^*)^{\alpha} \mathcal{J}_{iA}(\mathbf{X}^*) d\mathbf{X} + \int_K \sum_{|\alpha|=k_{\mathcal{K}}} \frac{1}{\alpha!} D_{\mathbf{X}}^{\alpha} \hat{f}^{**}(\mathbf{X} - \mathbf{X}^*)^{\alpha} \nabla_{\mathbf{X}} \mathcal{J}_{iA}^{**} \cdot (\mathbf{X} - \mathbf{X}^*) d\mathbf{X}$$

Since the volume of the reference element K is of an $\mathcal{O}(1)$, we need to estimate the derivatives of \hat{f} , and combine with the available estimates $\mathcal{J}_{iA}(\mathbf{X}^*) = \mathcal{O}(h^2)$, and $\nabla_{\mathbf{X}} \mathcal{J}_{iA}^{**} \cdot (\mathbf{X} - \mathbf{X}^*) = \mathcal{O}(h^2)$. To estimate the derivatives of \hat{f} we now use the fact that $|\nabla^{\alpha} f| = |D^{\alpha} f|$ and [\(60\)](#)-[\(61\)](#) and obtain:

$$|\nabla_{\mathbf{X}} f(\mathbf{x}(\mathbf{X}))| = |\mathbf{J}_A \nabla_{\mathbf{x}} f| \leq C_1 h |D_{\mathbf{x}}^1 f|$$

$$|\nabla_{\mathbf{X}}^2 f(\mathbf{x}(\mathbf{X}))| = |\nabla_{\mathbf{X}} \mathbf{J}_A \nabla_{\mathbf{x}} f + \mathbf{J}_A^2 \nabla_{\mathbf{x}}^2 f| \leq C_2 h^2 \max_{m \leq 2} |D_{\mathbf{x}}^m f|$$

$$|\nabla_{\mathbf{X}}^3 f(\mathbf{x}(\mathbf{X}))| = |\nabla_{\mathbf{X}}^2 \mathbf{J}_A \nabla_{\mathbf{x}} f + (\nabla_{\mathbf{X}} \mathbf{J}_A) \mathbf{J}_A \nabla_{\mathbf{x}}^2 f + 2 \mathbf{J}_A \nabla_{\mathbf{X}} \mathbf{J}_A \nabla_{\mathbf{x}}^2 f + \mathbf{J}_A^3 \nabla_{\mathbf{x}}^3 f| \leq C_2 h^3 \max_{m \leq 3} |D_{\mathbf{x}}^m f|$$

etc

The k th derivative can be shown by induction (omitted for brevity) to be bounded by

$$|D_{\mathbf{x}}^k \hat{f}| \leq C_k h^k \max_{m \leq k} |D_{\mathbf{x}}^m f|$$

so that the quadrature error for the term under consideration can be estimated to

$$\begin{aligned} |\mathcal{E}_{\mathcal{I}_1}| &\leq C_{\mathcal{I}}^1 \max_{k \leq k_{\mathcal{K}}} |D_{\mathbf{x}}^k f| h^{k_{\mathcal{K}}+2} + C_{\mathcal{I}}^1 \max_{k \leq k_{\mathcal{K}}+1} |D_{\mathbf{x}}^k f| h^{k_{\mathcal{K}}+3} \\ &\leq C_{\mathcal{I}_1} \max_{k \leq k_{\mathcal{K}}} |D_{\mathbf{x}}^k f| h^{k_{\mathcal{K}}+2} \end{aligned} \quad (67)$$

We can proceed in a similar manner for the other integrals in (40) to obtain:

$$\begin{aligned} \mathcal{I}_2 &= \int_{\mathcal{K}} (P_h \mathbf{I}) : \nabla_{\mathbf{x}} \varphi_i \mathbf{g}_{\alpha}^* d\mathbf{x} \Rightarrow |\mathcal{E}_{\mathcal{I}_2}| \leq C_{\mathcal{I}_2} \max_{k \leq k_{\mathcal{K}}} |D_{\mathbf{x}}^k f| h^{k_{\mathcal{K}}+1} \\ \mathcal{I}_3 &= \int_{\mathcal{K}} \nabla_{\mathbf{x}} P_h \cdot \varphi_i \mathbf{g}_{\alpha}^* d\mathbf{x} \Rightarrow |\mathcal{E}_{\mathcal{I}_3}| \leq C_{\mathcal{I}_3} \max_{k \leq k_{\mathcal{K}}} |D_{\mathbf{x}}^k f| h^{k_{\mathcal{K}}+1} \end{aligned}$$

Note that for these terms, the presence of the derivative in the physical space $\nabla_{\mathbf{x}}$ let the estimate one order of magnitude larger in h with respect to (67). Similarly for the line integral

$$\mathcal{I}_4 = \int_{\partial \mathcal{K}} P_h \mathbf{I} \mathbf{g}_{\alpha}^* \varphi_i \cdot \mathbf{n} ds \Rightarrow |\mathcal{E}_{\mathcal{I}_4}| \leq C_{\mathcal{I}_4} \max_{k \leq \partial k_{\mathcal{K}}} |D_{\mathbf{x}}^k f| h^{k_{\partial \mathcal{K}}+1}$$

By summing up the different integrals we have obtained for the Well Balanced correction (40) the following bound

$$|\epsilon_P^K| = |\mathcal{I}_1 + \mathcal{E}_{\mathcal{I}_1} + \mathcal{I}_2 + \mathcal{E}_{\mathcal{I}_2} + \mathcal{I}_3 + \mathcal{E}_{\mathcal{I}_3} + \mathcal{I}_4 + \mathcal{E}_{\mathcal{I}_4}| = |\mathcal{E}_{\mathcal{I}_1} + \mathcal{E}_{\mathcal{I}_2} + \mathcal{E}_{\mathcal{I}_3} + \mathcal{E}_{\mathcal{I}_4}| \leq Ch^{\min(k_{\mathcal{K}}+1, k_{\partial \mathcal{K}}+1)}$$

having used the fact that for exact quadrature the sum of all the integrals \mathcal{I}_j vanishes. This proves the result of the proposition. Note that the constant on the left actually depends on the integrand, so in particular on the pressure field and its derivatives, so it is bounded provided these are.

407

408 We perform a numerical verification with the values used for all the numerical simulations of the paper,
409 namely $k_{\mathcal{K}} = k_{\partial \mathcal{K}} = 3p$. We consider a smooth pressure field $P(\varphi, \lambda) = 2 + \sin(2\pi\varphi) \cos(2\pi\lambda)$ defined on
410 a spherical triangle which is successively refined halving the mesh size. In Figure (15) we check the order
411 of accuracy for $|\epsilon_P^K|$ computed as $|\epsilon_P^K|_{\infty} = \max_K |\epsilon_P^K|$. For P^1, P^2 we recover numerically the estimate of
412 Proposition (41), while for P^3 we measure one order less w.r.t such theoretical estimate.

413 Acknowledgments

414 Work partially funded by the Carib-Coast INTERREG project (<https://www.interreg-caraibes.fr/caribcoast>).
415 Some of the computations presented in this paper were carried out using the BRGM experimental testbed.

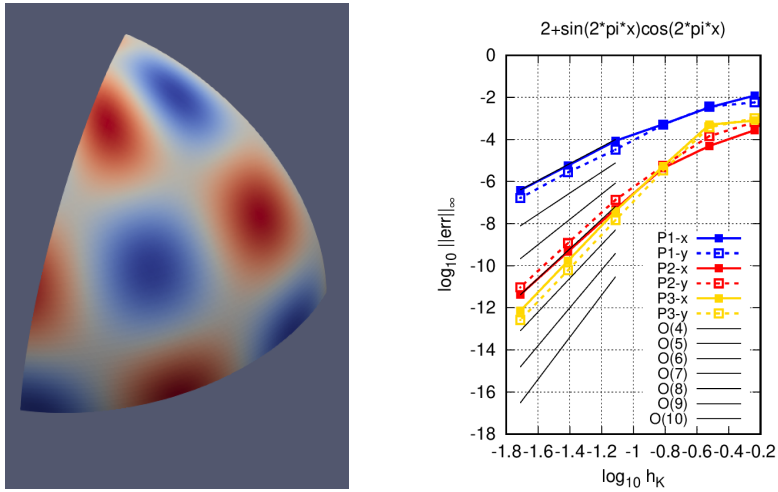


Figure 15: Numerical validation of the well balanced correction estimate for a smooth pressure field. Left: Domain and pressure field. Right: mesh convergence for $|e_P^K|_{\infty}$. The dashed and continuous lines represent the x and y components of the correction.

416 All the developments presented have been implemented in the platform **Aerosol/Uhaina** co-developed by
 417 EPOC, IMAG, IMB and INRIA. In particular we are very grateful to Vincent Perrier for the time ded-
 418 icated to us on the Aerosol library and for his availability all along the implementation of the present
 419 work.

420 References

- 421 [1] D. Williamson, The evolution of dynamical cores for global atmospheric models, *J. Meteorol. Soc.*
 422 *Jpn.* 85 (2007) 241–269.
- 423 [2] A. Kageyama, T. Sato, "Yin-Yang grid": An overset grid in spherical geometry, *Geochem. Geophys.*
 424 *Geosyst.* 5 (2004) Q09005.
- 425 [3] C. Ronchi, R. Iacono, P. S. Paolucci, The "cubed sphere": A new method for the solution of partial
 426 differential equations in spherical geometry, *J. Comput. Phys.* 124 (1996) 93–114.
- 427 [4] R. D. Nair, S. J. Thomas, R. D. Loft, A discontinuous galerkin transport scheme on the cubed sphere,
 428 *Monthly Weather Review* 133 (2004) 814–828.
- 429 [5] P. A. Ullrich, C. Jablonowski, B. Van-Leer, High-order finite-volume methods for the shallow water
 430 equations on the sphere, *J. Comput. Phys.* 229 (2010) 6104–6134.

- 431 [6] J. A. Rossmannith, A wave propagation method for hyperbolic systems on the sphere, *J. Comput.*
432 *Phys.* 213 (2006) 629–658.
- 433 [7] G. Madec, M. Imbard, A global ocean mesh to overcome the north pole singularity, *Climate Dynamics*
434 12 (1996) 381–388.
- 435 [8] J. Coté, A Lagrange multiplier approach for the metric terms of semi-Lagrangian models on the
436 sphere, *Quart. J. R. Met. Soc.* 114 (1988) 1347–1352.
- 437 [9] F. X. Giraldo, J. S. Hesthaven, T. Warburton, Nodal high-order discontinuous galerkin methods for
438 the spherical shallow water equations, *J. Comput. Phys.* 181 (2002) 499–525.
- 439 [10] P. E. Bernard, J. F. Remacle, R. Comblen, V. Legat, K. Hillewaert, High-order discontinuous Galerkin
440 schemes on general 2D manifolds applied to the shallow water equations, *J. Comput. Phys.* 228 (2009)
441 6514–6535.
- 442 [11] M. Baldauf, Discontinuous galerkin solver for the shallow-water equations in covariant form on the
443 sphere and the ellipsoid, *J. Comput. Phys.* 410 (109384) (2020) 1–26.
- 444 [12] S. P. A. Ern, K. Djadel, A well-balanced runge-kutta discontinuous galerkin method for the shallow-
445 water equations with flooding and drying, *Int. J. Numer. Meth. Fluids* 58 (2008) 1–25.
- 446 [13] Y. Xing, X. Zhang, Positivity-preserving well-balanced discontinuous galerkin methods for the shallow
447 water equations on unstructured triangular meshes, *Journal of Scientific Computing* 57 (2013) 19–41.
- 448 [14] S. Vater, N. Beisiegel, J. Behrens, A limiter-based well-balanced discontinuous galerkin method for
449 shallow-water flows with wetting and drying: Triangular grids, *Int. J. Numer. Meth. Fluids* 91 (2019)
450 395–418.
- 451 [15] R. Abgrall, M. Ricchiuto, High order methods for CFD, in: E. Stein, R. de Borst, T. J. R. Hughes
452 (Eds.), *Encyclopedia of Computational Mechanics*, Second Edition, John Wiley and Sons, 2017.
- 453 [16] M. Ricchiuto, An explicit residual based approach for shallow water flows, *J. Comput. Phys.* 80 (2015)
454 306–344.
- 455 [17] B. Bonev, J. S. Hesthaven, F. X. Giraldo, M. A. Kopera, Discontinuous galerkin scheme for the
456 shallow water equations with application to tsunami modeling and prediction, *J. Comput. Phys.* 362
457 (2018) 425–448.

- 458 [18] A. Bermudez, M. E. Vazquez-Cendon, Upwind methods for hyperbolic conservation laws with source
459 terms, *Comput. Fluids* 235 (8) (1994) 1049–1071.
- 460 [19] A. E. Gill, *Atmosphere-Ocean Dynamics*, Academic, San Diego, Calif., 1982.
- 461 [20] D. Mercer, J. Sheng, R. J. Greatbatch, J. Bobanovic, Barotropic waves generated by storms moving
462 rapidly over shallow water, *J. Geophys. Res.* 107 (C10) (2002) 16–1–16–17.
- 463 [21] F. Bouchut, J. LeSommer, V. Zeitlin, Frontal geostrophic adjustment and nonlinear-wave phenom-
464 ena in one dimensional rotating shallow water, *J. Fluid Mech. Part 2: High-Resolution Numerical
465 Simulations* 514 (2004) 35–63.
- 466 [22] D. Kopriva, Metric identities and the discontinuous spectral element method on curvilinear meshes,
467 *Journal of Scientific Computing* 26 (2006) 301–327.
- 468 [23] E. Audusse, F. Bouchut, M.-O. Bristeau, R. Klein, B. Perthame, A fast and stable well-balanced
469 scheme with hydrostatic reconstruction for shallow water flows, *SIAM Journal of Scientific Computing*
470 25 (2004) 2050–2065.
- 471 [24] J. L. Guermond, R. Pasquetti, B. Popov, Entropy viscosity method for nonlinear conservation laws,
472 *J. Comput. Phys.* 230 (2011) 4248–4267.
- 473 [25] R. Pasquetti, Viscous stabilizations for high order approximations of Saint-Venant and Boussinesq
474 flows, In *Global Tsunami Science: Past and Future*, Springer International Publishing, 2017, pp.
475 3671–3692.
- 476 [26] A. G. Filippini, S. D. Brye, V. Perrier, F. Marche, M. Ricchiuto, D. Lannes, P. Bonneton, UHAINA:
477 A parallel high performance unstructured near-shore wave model, *XVmes Journées Nationales Génie
478 Cotier - Génie Civil*. 2018.
- 479 [27] S. Gottlieb, C. W. Shu, E. Tadmor, Strong stability-preserving high-order time discretization meth-
480 ods, *SIAM Rev.* 43 (2001) 89–112.
- 481 [28] J. Hou, Q. Liang, F. Simons, R. Hinkelmann, A stable 2d unstructured shallow flow model for
482 simulations of wetting and drying over rough terrains, *Computers & Fluids* 82 (2013) 132–147.
- 483 [29] A. I. Delis, M. Kazolea, N. A. Kampanis, A robust high-resolution finite volume scheme for the
484 simulation of long waves over complex domains, *International Journal for Numerical Methods in
485 Fluids* 56 (4) (2008) 419–452.

- 486 [30] D. L. Williamson, J. B. Drake, J. J. Hack, R. Jakob, P. N. Swarztrauber, A standard test set for
487 numerical approximations to the shallow water equations in spherical geometry, *J. Comput. Phys.*
488 102 (1992) 211–224.
- 489 [31] J. Galewsky, R. K. Scott, L. M. Polvani, An initial-value problem for testing numerical models of
490 the global shallow-water equations, *Tellus A: Dynamic Meteorology and Oceanography* 56 (5) (2004)
491 429–440.
- 492 [32] L. Arpaia, M. Ricchiuto, Well-balanced residual distribution for the ALE spherical shallow water
493 equations on moving adaptive meshes, *J. Comput. Phys.* 405 (109173) (2020) 1–32.
- 494 [33] N. Feuillet, I. Manighetti, P. Tapponnier, E. Jacques, Arc parallel extension and localization of
495 volcanic complexes in Guadeloupe, Lesser Antilles, *J. Geophys. Res.* 107 (B12) (2002) 3–1–3–29.
- 496 [34] R. J. LeVeque, K. Waagan, F. I. Gonzalez, D. Rim, G. Lin, Generating random earthquake events for
497 probabilistic tsunami hazard assessment, In *Global Tsunami Science: Past and Future*, Birkhauser,
498 Cham., 2016, pp. 3671–3692.
- 499 [35] F. Shi, J. T. Kirby, J. C. Harris, J. D. Geiman, S. T. Grilli, A high-order adaptive time-stepping
500 TVD solver for boussinesq modeling of breaking waves and coastal inundation, *Ocean Modelling* 43-44
501 (2012) 36–51.
- 502 [36] H. Charnock, Wind stress on a water surface, *Quart. J. R. Met. Soc.* 81 (1955) 639–640.
- 503 [37] H. Muller, L. Pineau-Guillou, D. Idier, F. Ardhuin, Atmospheric storm surge modeling methodology
504 along the french (Atlantic and English Channel) coast, *Ocean Dyn.* 64 (11) (2014) 1671–1692.
- 505 [38] K. Knapp, M. Kruk, D. Levinson, H. Diamond, C. Neumann, The international best track archive for
506 climate stewardship (IBTrACS): unifying tropical cyclone best track data, *Bull. Am. Meteor. Soc.* 91
507 (2010) 363–376.
- 508 [39] G. Holland, An analytic model of the wind and pressure profiles in hurricanes, *Monthly Weather*
509 *Review* 108 (1980) 1212–1218.
- 510 [40] S. Saha, S. Moorthi, H. Pan, X. W. et al., The NCEP climate forecast system reanalysis, *Bull. Am.*
511 *Meteor. Soc.* 91 (2010) 1015–1057.

- 512 [41] W. Pringle, J. Gonzalez, B. Joyce, J. Westerink, A. J. van der Westhuysen, Baroclinic coupling
513 improves depth-integrated modeling of coastal sea level variations around Puerto Rico and the U.S.
514 Virgin Islands, *Journal of Geophysical Research: Oceans* 124 (3) (2019) 2196–2217.
- 515 [42] B. R. Joyce, J. Gonzalez, A. J. van der Westhuysen, D. Yang, W. J. Pringle, J. Westerink, U.S.
516 IOOS coastal and ocean modeling testbed: Hurricane-induced winds, waves, and surge for deep
517 ocean, reef-fringed islands in the Caribbean, *Journal of Geophysical Research: Oceans* 124 (3) (2019)
518 2876–2907.
- 519 [43] S. Michel, D. Torlo, M. Ricciuto, R. Abgrall, Spectral analysis of continuous FEM for hyperbolic
520 PDEs: influence of approximation, stabilization, and time-stepping (2021). [arXiv:2103.16158](https://arxiv.org/abs/2103.16158).
- 521 [44] P. G. Ciarlet, P.-A. Raviart, Interpolation theory over curved elements, with application to finite
522 element methods, *Comp. Meth. Appl. Mech. Eng.* 1 (1972) 217–249.
- 523 [45] L. Engvall, J. A. Evans, Mesh quality metrics for isogeometric Bernstein-Bezier discretizations, *Comp.*
524 *Meth. Appl. Mech. Eng.* 371 (2020) 113305.